

A meshless method with enriched weight functions for three-dimensional crack propagation

Marc DufLOT *

Abstract

The propagation of cracks in three dimensions is analyzed by a meshless method. The cracks are modeled by a set of triangles that are added when the propagation occurs. Since the method is meshless, no remeshing of the domain is necessary during the propagation. To avoid using a large number of degrees of freedom, the stress singularity along the front of the cracks is taken into account by an enrichment of the shape functions of the meshless method by means of appropriate weight functions. This enrichment technique is an extension of the technique that proved to be successful in two dimensions in a previous paper. Several algorithms for efficiently implementing the meshless method in three dimensions are detailed. The accuracy of the enrichment is first assessed on simple examples and some results of non-planar propagation of multiple cracks are then presented.

Key-words: meshless method; crack propagation; near-tip enrichment

1 INTRODUCTION

The meshless method is an alternative to the finite element method. It was introduced under the name *diffuse element method* in Reference [1] and developed under the name *element-free Galerkin method* in Reference [2] and in a large number of subsequent papers by Belytschko and co-workers. This method has been frequently used in crack growth simulations. As a matter of fact, it does not require a mesh to build the shape functions used to approximate the displacement field and so, there is no mesh to rebuild between each step of the propagation of cracks unlike the finite element method. Two other numerical methods share this advantage: the boundary element method (see Reference [3] for its application to three-dimensional crack propagation) and the extended finite element method (see References [4, 5]). In the recent years, the latter method has caught most of the attention that was previously on the meshless method within the computational fracture mechanics community. We intend to demonstrate in this paper that the meshless method remains an efficient way to solve fracture mechanics problems, even multiple non-planar cracks propagation.

Most of the papers about the meshless method in fracture mechanics concentrate on two-dimensional crack propagation problems. We cite below all the papers published about this matter to our knowledge, sorting them by school and then in chronological order.

The first papers are Reference [6] for quasi-static fracture, Reference [7] for fatigue fracture and References [8, 9, 10] for dynamic fracture. The method is improved in Reference [11] to be coupled with the finite element method in order to limit the meshless region to the vicinity of the crack. The method is modified in Reference [12] to ensure the continuity of the displacement field near the crack tip. Reference [13] is an overview of these early works. The method is enriched in Reference [14] to obtain an accurate approximation of the near-tip stress singularity. In Reference [15], an arbitrary Lagrangian-Eulerian formulation is proposed to relocate a set of nodes added near the crack tip when the crack grows under dynamic conditions. The method is used in Reference [16] for dynamic fracture in concrete. A level set representation of the crack instead of a broken line representation is used in Reference [17].

In Reference [18], quasi-static fracture problems are solved by a meshless method. Elastic and elasto-plastic fracture problems are studied respectively in References [19] and [20]. References [21, 22, 23, 24, 25] present in that order a method with an enriched set of basis functions, a method coupled to the finite element method and the application of that method to probabilistic fracture mechanics on one hand and to non-linear fracture mechanics on the other hand. A coupled finite element/meshless method with automatic inclusion of a meshless

*Correspondence to: Marc DufLOT, CENAERO, Avenue Jean Mermoz 30, 6041 Gosselies, Belgium. E-mail: marc.dufLOT@cenaero.be.

zone in the cracked region is presented in Reference [26]. An adaptive method is used in Reference [27] to add nodes near the crack tip according to an error estimator in order to accurately catch the stress singularity. In Reference [28], this stress singularity difficulty is addressed by means of an explicit enrichment and in Reference [29], we propose a new enrichment technique by means of the weight functions that we apply to multi-cracked bodies. Finally, a meshless method is used in Reference [30] in plasticity with an application to crack growth problems.

Only two papers concern the solution of three-dimensional crack problems by a meshless method: Reference [31] for plane non-propagating cracks and Reference [32] for the propagation of arbitrary cracks.

In the present paper, we model the propagation of multiple arbitrary cracks in three dimensions in an elastic body by using a meshless method with an improved accuracy by using the enrichment technique that takes into account the asymptotic displacement field near the front by means of the weight functions. This enriched technique proved to be successful in two dimensions in our previous paper [29]. In addition, we use the diffraction criterion proposed in Reference [12] in two dimensions that was never used before for arbitrary three-dimensional cracks. We also describe efficient algorithms to implement the meshless method that are mandatory to use the method in three dimensions in a moderate computational time.

The outline of the paper is as follows. The equations of the meshless method that are useful in the rest of the paper are given in Section 2. The crack representation and the way the meshless method takes into account the discontinuity of the displacement field across the crack are detailed in Section 3. The distribution of the nodes used to build the approximation of the displacement field for the non-enriched method is presented in Section 4. Section 5 is the main contribution of this paper. After reviewing techniques used in the literature to accurately catch the singularity of the stresses at the crack front, the enrichment of the meshless method by means of the weight functions in three dimensions is presented. The integration scheme to assemble the stiffness matrix and the computation of the stress intensity factors are briefly given in Sections 6 and 7 respectively for the purpose of reproducibility of the results. The evolution of the crack representation when the propagation occurs is described in Section 8. Efficient algorithms to implement the meshless method are presented in Section 9. Several numerical results are shown in Section 10. First, simple examples underline the improvement due to the enriched method with respect to the non-enriched method. Then, the enriched method is applied to single or multiple non-planar cracks propagations. The conclusions are drawn in Section 11.

2 MESHLESS METHOD

The meshless method for elastic problems consists in approximating the displacement field by a linear combination of some shape functions

$$\mathbf{u}^h(\mathbf{x}) = \sum_{i=1}^N \phi_i(\mathbf{x}) \mathbf{u}_i \quad (1)$$

and in introducing this approximation in the weak form of the equations of elasticity as in the finite element method. To the contrary of the latter method, the shape functions are built without recourse to a mesh by a moving-least square approximation (MLSA). We summarize the equations and properties of the MLSA below.

Consider a set of N nodes scattered in a domain Ω and let \mathbf{x}_i be the coordinates of node i . The MLSA $\mathbf{u}^h(\mathbf{x})$ of a (multi-dimensional) field $\mathbf{u}(\mathbf{x})$ in Ω is Equation (1) where \mathbf{u}_i is the value of the field \mathbf{u} at \mathbf{x}_i and ϕ_i is the shape function of node i , given by

$$\phi_i(\mathbf{x}) = \mathbf{c}^T(\mathbf{x}) \mathbf{p}(\mathbf{x}_i) w_i(\mathbf{x}) \quad (2)$$

where $\mathbf{p}(\mathbf{x})$ is a set of basis functions, $w_i(\mathbf{x})$ is a weight function associated with node i and

$$\mathbf{c}(\mathbf{x}) = \mathbf{A}^{-1}(\mathbf{x}) \mathbf{p}(\mathbf{x}) \quad (3)$$

with

$$\mathbf{A}(\mathbf{x}) = \sum_{i=1}^N w_i(\mathbf{x}) \mathbf{p}(\mathbf{x}_i) \mathbf{p}^T(\mathbf{x}_i) \quad (4)$$

In practice, the weight functions are positive so that the \mathbf{A} matrix is definite positive and that the approximation is well-behaved. Moreover, a small domain Ω_i containing \mathbf{x}_i is associated with node i such that $w_i(\mathbf{x})$, and as a result $\phi_i(\mathbf{x})$, vanish outside Ω_i . This choice is made in order to give the approximation a local character and to restrict the sums in Equations (1) and (4) to a few terms. Finally, the common choice in the literature is that $w_i(\mathbf{x})$ decreases with the distance between \mathbf{x}_i and \mathbf{x} , in such a way that the nearer a node is to a point, the greater it influences this point; but, this choice is revised in Section 5.

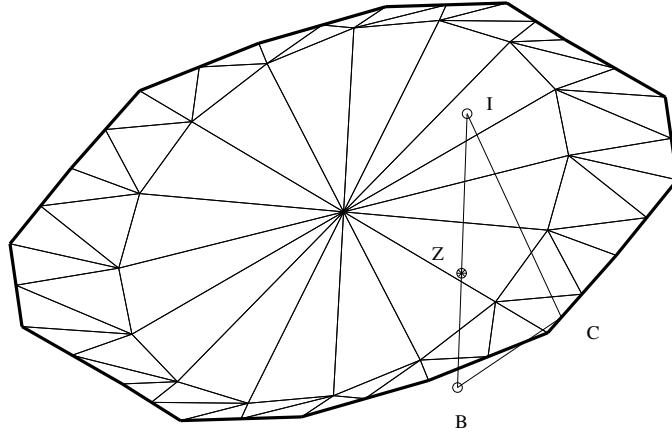


Figure 1: The crack model and the distances used for the visibility, diffraction and transparency criteria.

As in two dimensions in Reference [29], we use a linear basis: $\mathbf{p}^T = [1, x, y, z]$, and the same weight for each regular node (in contrast with the enriched nodes described later): a quartic weight function on a spherical support

$$w_i(\mathbf{x}) = S_4(s) \quad (5)$$

where S_4 is the quartic spline

$$S_4(s) = \begin{cases} 1 - 6s^2 + 8s^3 - 3s^4 & \text{if } s \leq 1 \\ 0 & \text{if } s > 1 \end{cases} \quad (6)$$

and the normalized distance is

$$s = \frac{\|\mathbf{x} - \mathbf{x}_i\|}{R_i} \quad (7)$$

with R_i the radius of the influence domain of node i .

3 CRACK MODEL

3.1 Crack representation

Usually, a crack in two dimensions is modeled by a set of successive linear segments. In this paper, the representation of a three-dimensional crack is also piecewise linear: the crack is modeled by a set of joined triangles. The description of the front by a path of linear segments is also necessary. An example of an initially circular crack, submitted to tension in a direction inclined with its normal, after a one-step growth, is shown in Figure 1. The crack surface is modeled by a set of 64 triangles and the crack front is modeled by a path of 16 segments, which are plotted in bold.

3.2 Discontinuity of the displacement field

Cracks in a solid are internal boundaries across which the displacement field is discontinuous. These are geometrical discontinuities, as opposed to the material discontinuities that are the boundary between dissimilar materials. In order to obtain an accurate solution, it is indispensable that the approximation of the displacement takes into account these discontinuities. Before explaining the techniques by which these discontinuities may be introduced into the meshless method, we review the way to do it in the other numerical methods.

In the classical finite element method, the mesh matches the internal boundaries. The nodes on a crack are divided into two and the shape function of each node is non-zero only on one side of this crack. The displacement is naturally discontinuous since no shape function in the approximation

$$\mathbf{u}(\mathbf{x}) = \sum_{i=1}^N \phi_i(\mathbf{x}) \mathbf{q}_i \quad (8)$$

extends to both sides of the crack (except for the nodes on the crack fronts).

In the extended finite element method, the mesh does not match the internal boundaries. Degrees of freedom are added at each node with a support cut by a crack. The shape functions associated with these new degrees of freedom are the regular shape functions multiplied by a step function H with a changing sign across the cracks. If we omit the near-tip field enrichment, the displacement approximation is expressed as

$$\mathbf{u}(\mathbf{x}) = \sum_{i=1}^N \phi_i(\mathbf{x}) \mathbf{q}_i + \sum_j \phi_j(\mathbf{x}) H(\mathbf{x}) \mathbf{b}_j \quad (9)$$

where the second sum is on the nodes belonging to an element cut by a crack. The degrees of freedom \mathbf{b}_j give the opening of the displacement field along the cracks. This technique is also used for the meshless method in Reference [17].

In the boundary element method, the displacement at an interior point is obtained by integration on the whole boundary of a function that is singular when the point reaches the boundary. This singularity is such that the displacement is discontinuous across the internal boundaries.

In the meshless method, the discontinuity is introduced in the shape functions ϕ of the approximation (1) by means of the weight functions w . If there is no crack, the weight function of a node at a point increases with the proximity of this point. If there are cracks, the proximity concept is modified to take them into account. There is a screening effect that diminishes the weight a node has at a point if the cracks hide this point. Five criteria exist in the literature for two-dimensional crack modeling:

- the visibility criterion in the initial paper [2],
- the diffraction criterion in Reference [12],
- the transparency criterion in the same paper [12],
- the wedge model in Reference [33],
- the virtual crack extension model in Reference [34].

For three-dimensional crack modeling, the first two criteria are presented in Reference [31] for plane cracks and only the visibility criterion is used in Reference [32] for arbitrary cracks. We describe below the visibility, diffraction and transparency criterion for arbitrary cracks with the help of Figure 1 and indicate our choice.

Visibility criterion The weight of node I at point B is set to zero if the segment that joins them is cut by a crack. This criterion gives the discontinuity of the shape functions across the crack but also across a large number of surfaces that pass by a node and a front segment. It is shown in Reference [35] that the convergence of the solution is guaranteed even with these discontinuities. But, it is shown in Reference [12] that smoother criteria are more efficient in two dimensions.

Diffraction criterion If the segment that joins node I to point B is cut by a crack, the normalized distance (7) in the definition of the weight function is replaced by the normalized length of the shortest path from I to B passing by a point of the front (ICB in Figure 1):

$$s = \frac{\|\mathbf{x} - \mathbf{x}_c\| + \|\mathbf{x}_c - \mathbf{x}_i\|}{R_i} \quad (10)$$

The weight function of node I is then continuous except across the crack.

Transparency criterion If the segment that joins node I to point B is cut by a crack, the normalized distance (7) is augmented by a transparency function that increases with the distance between the front and the intersection of the segment with the crack (point Z in Figure 1)

$$s = \frac{\|\mathbf{x} - \mathbf{x}_i\|}{R_i} + f_t(\|\mathbf{x}_z - \mathbf{x}_c\|) \quad (11)$$

with $f_t(0) = 0$ and f_t a strictly increasing function to choose.

According to our experience and the observations of Reference [36], the visibility criterion has spurious discontinuities and the transparency criterion gives sharply varying shape functions for the nodes near the crack. So, we decide to use the diffraction criterion.

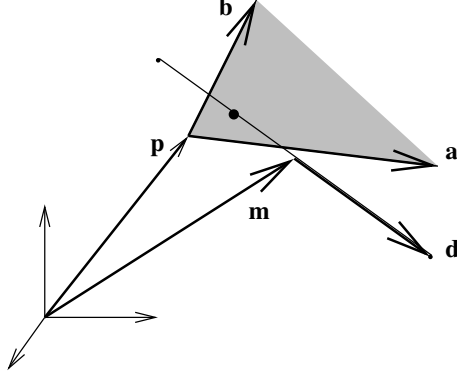


Figure 2: Position vectors and direction vectors of a line segment and triangle

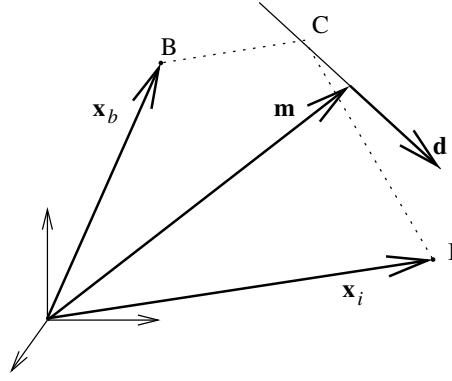


Figure 3: Path from I to B that passes by a line segment

3.3 Implementation of the diffraction criterion

The main task in implementing the diffraction criterion is the count of the number of intersections between a segment and a set of triangles. For each node and each integration point, we consider the segment joining them and make a loop on all the triangles. The segment defined by a position vector \mathbf{m} and a direction vector \mathbf{d} intersects a triangle defined by a position vector \mathbf{p} and direction vectors \mathbf{a} and \mathbf{b} (see Figure 2) if all the following conditions are met ($[\mathbf{x}, \mathbf{y}, \mathbf{z}]$ is the scalar triple product $(\mathbf{x} \wedge \mathbf{y}) \cdot \mathbf{z}$):

$$\frac{[\mathbf{m} - \mathbf{p}, \mathbf{b}, -\mathbf{d}]}{[\mathbf{a}, \mathbf{b}, -\mathbf{d}]} \geq 0 \quad (12)$$

$$\frac{[\mathbf{a}, \mathbf{m} - \mathbf{p}, -\mathbf{d}]}{[\mathbf{a}, \mathbf{b}, -\mathbf{d}]} \geq 0 \quad (13)$$

$$\frac{[\mathbf{m} - \mathbf{p}, \mathbf{b}, -\mathbf{d}]}{[\mathbf{a}, \mathbf{b}, -\mathbf{d}]} + \frac{[\mathbf{a}, \mathbf{m} - \mathbf{p}, -\mathbf{d}]}{[\mathbf{a}, \mathbf{b}, -\mathbf{d}]} \leq 1 \quad (14)$$

$$-1 \leq \frac{[\mathbf{a}, \mathbf{b}, \mathbf{m} - \mathbf{p}]}{[\mathbf{a}, \mathbf{b}, -\mathbf{d}]} \leq 1 \quad (15)$$

If the number of intersections is zero or even, the node and the point are on the same side of the crack and then the distance used in the weight function is not modified. If this number is odd, we must find the shortest path between the node and the point that passes by the front. To that end, we make a loop on all the front segments, compute the length of the path between the node and the point that passes by this segment and retain the minimal length. The length of this path is computed as follows.

Consider node I, point B, and a given front segment defined by (see Figure 3):

$$\mathbf{m} + l\mathbf{d} = 0 \quad (16)$$

with l varying from -1 to 1 . The nearest points on the line containing the segment to node I and point B are

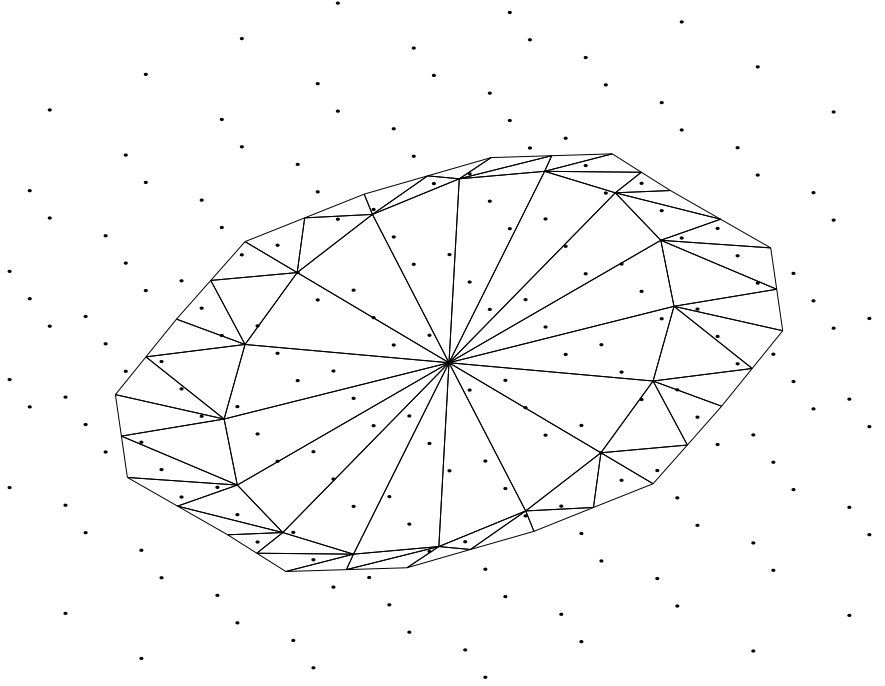


Figure 4: Regular nodal distribution

respectively at the following coordinates:

$$l_i = \frac{(\mathbf{x}_i - \mathbf{m}) \cdot \mathbf{d}}{\|\mathbf{d}\|^2} \quad l_b = \frac{(\mathbf{x}_b - \mathbf{m}) \cdot \mathbf{d}}{\|\mathbf{d}\|^2} \quad (17)$$

The distances between the line containing the segment and node I on one hand and point B on the other hand are respectively

$$d_i = \|\mathbf{m} + l_i \mathbf{d} - \mathbf{x}_i\| \quad d_b = \|\mathbf{m} + l_b \mathbf{d} - \mathbf{x}_i\| \quad (18)$$

The coordinate of pivot C by which the shortest path between I and B passes is:

$$l_c = \frac{d_a l_b + d_b l_a}{d_a + d_b} \quad (19)$$

If $l_c > 1$ (resp. $l_c < -1$), l_c is changed to 1 (resp. -1) to stay on the segment. The position of the pivot is

$$\mathbf{x}_c = \mathbf{m} + l_c \mathbf{d} \quad (20)$$

The length of the shortest path from I and B that passes on the segment is finally

$$\|\mathbf{x}_c - \mathbf{x}_i\| + \|\mathbf{x}_c - \mathbf{x}_b\| \quad (21)$$

The implementation of the diffraction criterion in three dimensions is quite expensive. To reduce the computational cost, before each step of the simulation of the propagation, we associate with each node the list of the cracks that cut the support of this node (i.e. if the distance from the node to a crack is lower than the radius of the influence domain). So, it is only necessary to apply the algorithm of the diffraction criterion for the affected nodes.

4 NODAL DISTRIBUTION

We use as a basis for the construction of the shape functions a regular nodal distribution, with constant spacing h (see Figure 4). Of course, it would be more efficient to concentrate the nodes near the crack front where the stresses are singular. But, that nodal distribution would require to be modified at each step of the propagation. In addition, we do not want to guess beforehand where the cracks will grow and refine these areas. We explain in the next section the way we treat the singularities.

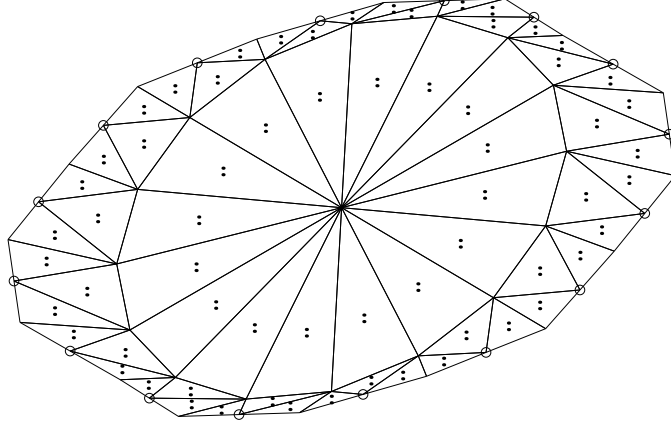


Figure 5: Additional nodes

The MLSA with a linear basis is well-defined if each point is covered by at least four influence domains, provided that the four nodes are not in the same plane. With a regular grid of nodes, it is easy to choose the radius of the influence domains to satisfy that condition. It is sufficient for each radius to be greater than h . We choose $R_i = 1.4h$.

In the presence of cracks, there are two corrections to make to the regular distribution as in Reference [29] in two dimensions. First, if a node is located on a crack surface, it is duplicated; one node is moved of a small distance at one side of the crack and the other is moved of the same amount at the other side. Second, some nodes are added near the crack surfaces at each side of the cracks. Without these nodes, some points near the crack surfaces would not be covered by a sufficient number of influence domains when the diffraction (or another) criterion is used. We choose to add these nodes at the center of each triangle modeling the crack surfaces. These additional nodes are the dots in Figure 5.

5 ENRICHMENT NEAR THE CRACK FRONT

Our aim is to take into account in the approximation of the displacement field the leading terms of the near-tip asymptotic expansion of the displacement:

$$\mathbf{u}(\mathbf{x}) = K_I \mathbf{Q}_I(\mathbf{x}) + K_{II} \mathbf{Q}_{II}(\mathbf{x}) + K_{III} \mathbf{Q}_{III}(\mathbf{x}) \quad (22)$$

$$\mathbf{Q}_I(\mathbf{x}) = \frac{1}{2\mu} \sqrt{\frac{r}{2\pi}} \begin{pmatrix} \cos\left(\frac{\theta}{2}\right) [\kappa - 1 + 2 \sin^2\left(\frac{\theta}{2}\right)] \\ \sin\left(\frac{\theta}{2}\right) [\kappa + 1 - 2 \cos^2\left(\frac{\theta}{2}\right)] \\ 0 \end{pmatrix} \quad (23)$$

$$\mathbf{Q}_{II}(\mathbf{x}) = \frac{1}{2\mu} \sqrt{\frac{r}{2\pi}} \begin{pmatrix} \sin\left(\frac{\theta}{2}\right) [\kappa + 1 + 2 \cos^2\left(\frac{\theta}{2}\right)] \\ \cos\left(\frac{\theta}{2}\right) [-\kappa + 1 + 2 \sin^2\left(\frac{\theta}{2}\right)] \\ 0 \end{pmatrix} \quad (24)$$

$$\mathbf{Q}_{III}(\mathbf{x}) = \frac{1}{\mu} \sqrt{\frac{2r}{\pi}} \begin{pmatrix} 0 \\ 0 \\ \sin\left(\frac{\theta}{2}\right) \end{pmatrix} \quad (25)$$

where r and θ are the polar coordinates of \mathbf{x} in the normal plane to the front passing by \mathbf{x} with the angle measured from a line ahead of the crack front. K_I , K_{II} and K_{III} are the stress intensity factors of the opening, sliding and tearing modes respectively. μ is the shear modulus and κ is the Kolosov constant.

5.1 Review of existing methods

For two-dimensional cracks, Reference [14] proposes two enrichment techniques. First, the enrichment of the trial functions consists in adding two terms (in two dimensions) to the displacement approximation for each tip:

$$\mathbf{u}^h(\mathbf{x}) = \sum_{i=1}^N \phi_i(\mathbf{x}) \mathbf{u}_i + \sum_{j=1}^{n_c} \left[\mathbf{Q}_I^j(\mathbf{x}) k_I^j + \mathbf{Q}_{II}^j(\mathbf{x}) k_{II}^j \right] \quad (26)$$

where n_c is the number of crack tips and k_I^j and k_{II}^j are additional degrees of freedom associated with mode I and mode II respectively at tip j . The method works well in two dimensions but comes at the cost of an increase in the bandwidth of the stiffness matrix because the additional degrees of freedom interact with every other degrees of freedom. To reduce this cost, it is necessary to restrict the enrichment in regions surrounding the crack tip and to manage an enriched region, a transition region and a non-enriched region. This method does not seem to be easily extensible in three dimensions where the stress intensity factors vary along the front.

Second, the enrichment of the basis consists in adding terms to the linear basis since the MLSA can exactly represent each function in its basis. The basis used in Reference [14] in two dimensions is

$$\mathbf{p}^T = \left[1, x, y, \sqrt{r} \cos\left(\frac{\theta}{2}\right), \sqrt{r} \sin\left(\frac{\theta}{2}\right), \sqrt{r} \sin\left(\frac{\theta}{2}\right) \sin(\theta), \sqrt{r} \cos\left(\frac{\theta}{2}\right) \sin(\theta) \right] \quad (27)$$

of size 7 because every function in Equations (23) to (25) can be expressed as a linear combination of these functions. In Reference [21], this fully enriched basis is used and compared to the partially enriched basis

$$\mathbf{p}^T = [1, x, y, \sqrt{r}] \quad (28)$$

of size 4. These methods work well, particularly the fully enriched basis, but this latter method is quite computationally expensive because a 7×7 matrix must be inverted at each Gauss point (see Equations (3) and (4)) instead of a 3×3 matrix as it is the case with the linear basis. Again, it is possible to restrict the enrichments in regions surrounding the crack tips to reduce this cost. A fully enriched basis of size 8 is used in three dimensions for non-propagating plane cracks in Reference [31] (basis (27) plus z).

5.2 Enrichment by means of the weight functions

In this paper, we use the enrichment method by means of the weight functions proposed in two dimensions in Reference [29]. The principle of the method in two dimensions is to add some nodes with a radial variation in \sqrt{r} and an angular variation in $\cos\left(\frac{\theta}{2}\right)$ or $\sin\left(\frac{\theta}{2}\right)$ to the set of regular nodes. It is illustrated in Reference [29] that the resulting shape functions have the same kind of spatial variation than these new weights. The approximation space is thus enriched with shape functions that behave like the displacement field we want to approximate. There is a similarity between this technique of enriching the set of shape functions with the near-tip displacement field and the crack modeling with discontinuous shape functions by one of the criteria described in Section 3: in both cases, the expected behavior is introduced in the weight functions and is found in the shape functions.

In two dimensions, the crack lips are modeled by curves and the crack tips are points. The enrichment is introduced by placing some nodes with a special weight at each tip. But, in three dimensions, the crack faces are modeled by surfaces and the crack front is modeled by a curve. It is necessary to place these nodes at several locations on the front. The union of the spherical enriched domains centered on several points of the front forms a kind of enriched tube surrounding the front. The degrees of freedom associated with the enriched shape functions will vary from one enriched node to another. So, the approximation will be able to represent varying stress intensity factors and a varying crack opening along the front. We decide to put enriched nodes at the ends of each front segments as shown by the circles in Figure 5.

We use the following criteria to guide us in the choice of the special weight functions:

1. The weight functions should vary as \sqrt{r} for small r : this is the main criterion in order to obtain by derivation a stress field that varies as $\frac{1}{\sqrt{r}}$ for small r .
2. They should be positive: this is requested for the positive definiteness of the \mathbf{A} matrix.
3. They should have an angular variation of the same kind as those in Equations (23), (24) and (25): this suggests using $\cos\left(\frac{\theta}{2}\right)$ and $\sin\left(\frac{\theta}{2}\right)$.
4. They should be zero outside a circular support like the regular weights: this provides the enrichment with a local character.

The three nodes that are added at the points of the front have similar weights to those used in two

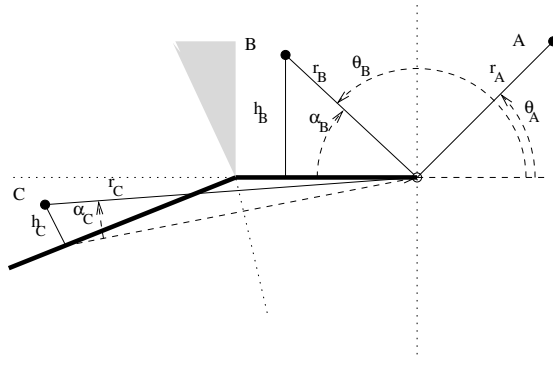


Figure 6: Angular mapping for a kinked crack

dimensions :

$$w_c(\mathbf{x}) = \alpha \sqrt{\frac{r}{R_{enr}}} \cos\left(\frac{\theta'}{2}\right) S_4(s) \quad (29)$$

$$w_p(\mathbf{x}) = \alpha \sqrt{\frac{r}{R_{enr}}} \left[1 + \sin\left(\frac{\theta'}{2}\right)\right] S_4(s) \quad (30)$$

$$w_m(\mathbf{x}) = \alpha \sqrt{\frac{r}{R_{enr}}} \left[1 - \sin\left(\frac{\theta'}{2}\right)\right] S_4(s) \quad (31)$$

where

- the indices c , p and m respectively stand for ‘cos’, ‘plus sin’ and ‘minus sin’,
- S_4 is the quartic spline function of Equation (6) and s is the normalized distance to the enriched node while r is the shortest distance to the front, which is measured in the normal plane to the front that passes by the current point (to the contrary of the two-dimensional case, $s \neq \frac{r}{R_{enr}}$),
- the mapped angle θ' is also measured in this plane and is described below,
- the radius R_{enr} must be large enough so that there is an overlap between the spheres that are the support of two neighboring enriched nodes,
- the α factor controls the amplitude of the enriched weights compared with the amplitude of the regular nodes; $\alpha = 1$ is a reasonable choice.

In two dimensions, we chose in Reference [29] to limit the radius of the enriched nodes to the distance between the tip and the first crack kink so that the enriched domain does not contain any kink. As a consequence, $\theta \in [-\pi, \pi]$. For non-planar cracks in three dimensions, we can not choose a small radius for the enriched spheres to be sure that this condition holds. A mapping of the polar angle in the normal planes to the crack front is necessary. Angle θ must be changed in θ' that equals π on one face and $-\pi$ on the other one to ensure that the discontinuities occur on the crack faces and not on their extension. We define θ' as follows :

$$\theta' = \begin{cases} \theta & \text{if } -\frac{\pi}{2} \leq \theta \leq \frac{\pi}{2} \\ \pi - \arcsin\left(\frac{h}{r}\right) & \text{above the crack} \\ -\pi + \arcsin\left(\frac{h}{r}\right) & \text{below the crack} \end{cases} \quad (32)$$

with h being the distance to the crack in the current normal plane. Several cases are illustrated in Figure 6 in two dimensions:

- For point A in front of the crack, $\theta'_A = \theta_A$.
- For point B above the crack and in front of the kink, $\theta'_B = \pi - \alpha_B$ with α_B measured from the crack, so $\theta'_B = \theta_B$.
- For point C above the crack but behind the kink, the mapping is applied and θ'_C is slightly smallest than π although θ_C is negative.

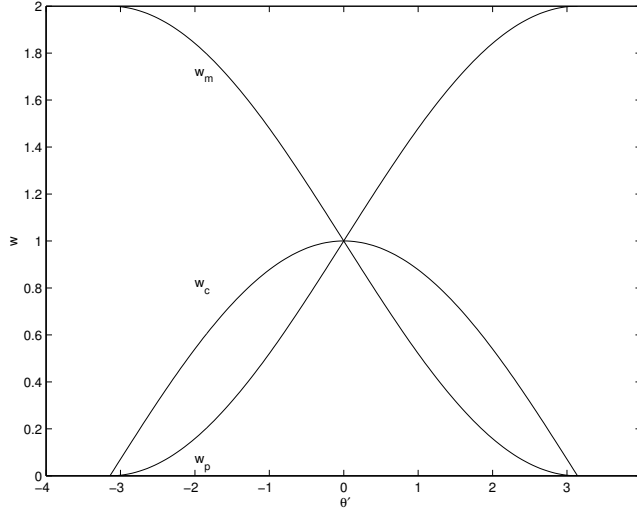


Figure 7: Enriched weight as a function of the angle

- As the point approaches the upper face, $h \rightarrow 0_+$ and thus $\theta' \rightarrow \pi$.

Was the mapping not applied, the weight functions would have been discontinuous across the dotted horizontal line. θ' is continuous across the dotted vertical line where $r = h$, so $\theta' = \pm \frac{\pi}{2}$. θ' is constant in the shaded area above the crack and with discontinuous derivatives across the inclined dotted line below the crack but the mapping is actually continuous everywhere.

With the help of the plot 7 of the three weights (29), (30) and (31) for a fixed r and of the plot 8 of any of these weights for a fixed θ' , we conclude that they meet the previous criteria :

1. At $r = 0$, the partial derivatives of the special weight functions $\frac{\partial w_{c,p,m}}{\partial r}$ are dominated by a term proportional to $\frac{1}{\sqrt{r}}$. These derivatives appear in the derivatives of the shape function by derivation of Equation (2), which in turn provide the desired singularity to the stress field.
2. They are positive since the quartic spline is positive and so are $\cos\left(\frac{\theta'}{2}\right)$, $1 + \sin\left(\frac{\theta'}{2}\right)$ and $1 - \sin\left(\frac{\theta'}{2}\right)$ ($\theta' \in [-\pi, \pi]$).
3. The three special weight functions are dominant in three different areas around the tip. w_c is dominant in front of the crack, w_p is dominant on the side of the crack where $\theta' = \pi$ and w_m is dominant on the other side where $\theta' = -\pi$. Moreover, w_p and w_m are discontinuous across the crack.
4. As $s \rightarrow 1$, $S_4 \rightarrow 0$ and the spline is the leading factor. The presence of the spline provides the local character of the special functions.

6 VOLUME INTEGRATION

The domain is divided into cells that are aligned on the regular nodal distribution. A Gaussian integration is performed in each cell to compute the stiffness matrix and the contribution of the body forces to the load vector. As illustrated in Figure 9, this division does not match the crack faces: some cells are cut by the crack. So, the integrands in these cells are discontinuous across the crack. Moreover, because of the enrichment, some integrands in the cells that contain a part of the crack front are singular in $\frac{1}{r}$ since they are proportional to the product of the derivatives (that behave like $\frac{1}{\sqrt{r}}$) of the shape functions (that behave like \sqrt{r}).

It is then necessary to take special care to accurately evaluate these discontinuities and singularities. In two dimensions, Reference [33] suggests using a subdivision of the cells that are cut by the crack into smaller cells that match the crack. So, this technique requires a kind of remeshing of the domain that we generally want to avoid if we use a meshless method. According to Reference [36] this technique does not significantly improve the accuracy with respect to the simple method of using a large number of Gauss points. In three dimensions, in Reference [31], only penny-shaped or straight cracks are analyzed and thus, the cells match the crack faces. In that paper, $6 \times 6 \times 6$ Gauss points are used in each cell and the quadrature scheme is not

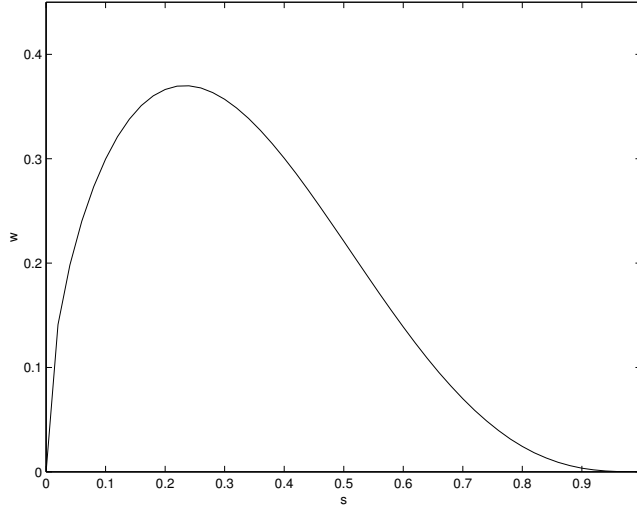


Figure 8: Enriched weight as a function of the distance

refined near the crack front although some integrands are singular because of the terms in \sqrt{r} in the enriched basis (27). In Reference [14], only $2 \times 2 \times 2$ Gauss points are used in each cell and it is written that the cells are subdivided into smaller ones when necessary but the criterion for the subdivision is not provided. In this paper, we also use the simple method and put $8 \times 8 \times 8$ Gauss points in each cell.

7 STRESS INTENSITY FACTORS COMPUTATION

At each step of the simulation, stress intensity factors at several points of the front need to be extracted from the solution. We evaluate the stress intensity factors at the ends of each front segment. At these points, a coordinate system is placed, with the x axis in the normal plane to the front ahead of the crack, the y axis in the same plane and normal to the crack and the z axis orthogonal to x and y (Figure 10). The stress intensity factors are computed by the interaction integral method of Reference [37], using the domain form of Reference [38]:

$$K_I = -\frac{E}{2(1-\nu^2)} \int_V \left[W^{(\text{sol},\text{I})} \frac{\partial q}{\partial x} - \left(\sigma_{ij}^{(\text{sol})} \frac{\partial u_i^{(\text{I})}}{\partial x} - \sigma_{ij}^{(\text{I})} \frac{\partial u_i^{(\text{sol})}}{\partial x} \right) \frac{\partial q}{\partial x_j} \right] dV \quad (33)$$

$$K_{II} = -\frac{E}{2(1-\nu^2)} \int_V \left[W^{(\text{sol},\text{II})} \frac{\partial q}{\partial x} - \left(\sigma_{ij}^{(\text{sol})} \frac{\partial u_i^{(\text{II})}}{\partial x} - \sigma_{ij}^{(\text{II})} \frac{\partial u_i^{(\text{sol})}}{\partial x} \right) \frac{\partial q}{\partial x_j} \right] dV \quad (34)$$

$$K_{III} = -\mu \int_V \left[W^{(\text{sol},\text{III})} \frac{\partial q}{\partial x} - \left(\sigma_{ij}^{(\text{sol})} \frac{\partial u_i^{(\text{III})}}{\partial x} - \sigma_{ij}^{(\text{III})} \frac{\partial u_i^{(\text{sol})}}{\partial x} \right) \frac{\partial q}{\partial x_j} \right] dV \quad (35)$$

where (sol) is the obtained numerical solution, (I), (II) and (III) are the leading terms of the near-tip asymptotic expansion of the unit mode I, II and III fields respectively and $W^{(\text{sol},\text{X})} = \sigma_{ij}^{(\text{sol})} \epsilon_{ij}^{(\text{X})}$.

The domain V is a rectangular box centered on the point of the front and aligned with the coordinate system (Figure 10). The weight q must equal 1 on the point of the front where we compute the factors and 0 on the boundary of V . We use the following weight

$$q = \left(1 - \frac{|x|}{\frac{c}{2}} \right) \left(1 - \frac{|y|}{\frac{c}{2}} \right) \left(1 - \frac{|z|}{\frac{l}{2}} \right) \quad (36)$$

where c is the size of the box in the x and y directions and l in the z direction. The integration is performed by dividing the box in $2 \times 2 \times 2$ cells with $8 \times 8 \times 8$ Gauss points in each.

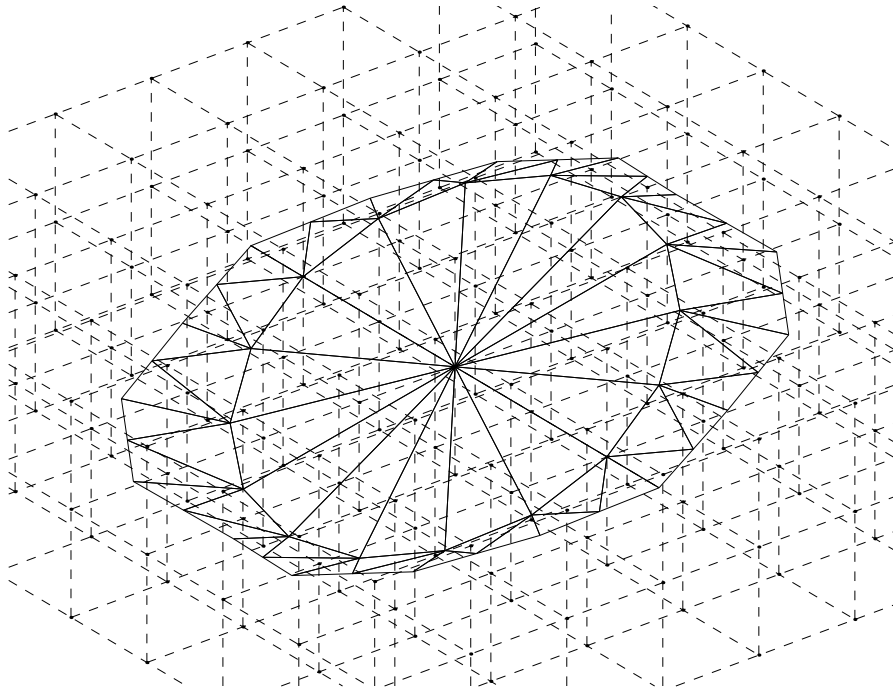


Figure 9: Division in integration cells

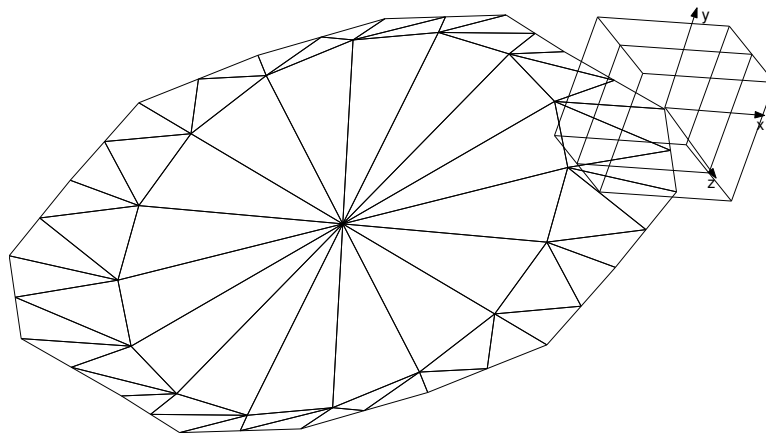


Figure 10: Coordinate system and domain for the stress intensity factors computation

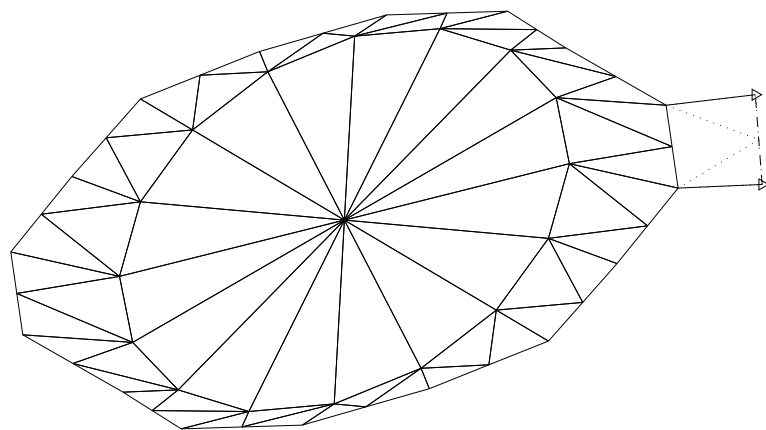


Figure 11: Crack propagation

8 CRACK PROPAGATION

The propagation of three-dimensional cracks is modeled by determining the new position of the ends of the front segments where the stress intensity factors are computed. These new points are then joined to build the new front and triangles are added between the old front and the new one. The new position of the ends of the front segments are located in the xy plane that is normal to the front at the point. The propagation direction with respect to the x axis and the length of the crack increment are determined by extending the method we used in two dimensions in Reference [29]. We assume that mode III does not affect the propagation direction and set this direction by using the maximum principal stress criterion in the xy plane:

$$\theta_p = 2 \arctan \left(\frac{K_I - \sqrt{K_I^2 + 8K_{II}^2}}{4K_{II}} \right) \quad (37)$$

On the contrary, mode III is taken into account in the propagation intensity. The Paris law is used:

$$\frac{da}{dN} = C (\Delta K_{Ieq})^m \quad (38)$$

where K_{Ieq} is the equivalent mode I stress intensity factor of the mixed three-mode state. For a mixed mode I and mode II state, the equivalent mode I stress intensity factor is

$$K_{Ieq}^{I,II} = K_I \cos^3 \frac{\theta_p}{2} - 3K_{II} \cos^2 \frac{\theta_p}{2} \sin \frac{\theta_p}{2} \quad (39)$$

The equivalent mode I stress intensity factor of the mixed three-mode state is taken as the stress intensity factor of the mode I that gives the same energy release rate as the combination of the mode III and the equivalent stress intensity factor of the two-dimensional theory:

$$K_{Ieq} = \sqrt{\left(K_I \cos^3 \frac{\theta_p}{2} - 3K_{II} \cos^2 \frac{\theta_p}{2} \sin \frac{\theta_p}{2} \right)^2 + \frac{E}{(1-\nu^2)2\mu} K_{III}^2} \quad (40)$$

A review of other criteria for crack path prediction in three dimensions can be found in Reference [39].

The increment lengths at the points of the front are obtained from the equivalent stress intensity factors at these points by integrating the Paris law in the same way than in two dimensions for several tips. The increment at the point with the maximum equivalent stress intensity factor K_{Ieq}^{\max} is set to a given value Δa_{\max} . The increments at the other points are shorter and given by:

$$\Delta a = \Delta a_{\max} \left(\frac{\Delta K_{Ieq}}{K_{Ieq}^{\max}} \right)^m \quad (41)$$

In the numerical examples, we take $m = 3.32$.

Figure 11 illustrates the propagation method. The new position of two neighboring points of the front are shown by two arrows. The dashed line is the new front segment that joins these new positions. The number of front segments is kept constant. Three new triangles are built to mesh the quadrangle formed by the old positions and the new ones. They are plotted in dotted line. The new crack surface after this method is applied to the whole front is shown in Figure 12. There are two ways to mesh the quadrangle with only two triangles but we prefer to use three triangles to preserve symmetry.

9 IMPLEMENTATION ISSUES

The shape functions and their derivatives must be evaluated at a large number of integration points during the assembling of the stiffness matrix and the computation of the stress intensity factors. This section presents two key aspects to efficiently implement the meshless method in three dimensions: a structure to quickly find which nodes contribute to the approximation at a given point and an algorithm to compute the shape functions.

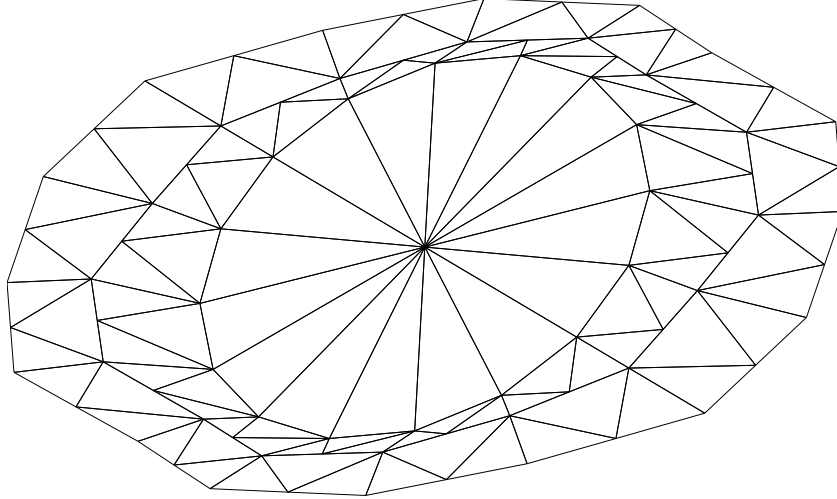


Figure 12: New crack

9.1 Octree structure

Beyond a certain number of nodes, it is absolutely essential to quickly determine which nodes influence a given point. These are the nodes with a non-zero weight at the point. They contribute to the \mathbf{A} matrix by Equation (4) and give a non-zero shape function by Equation (2). To that end, we use an octree that covers the domain Ω . Related papers are Reference [40] where an octree is used to build the set of influence domains for a partition of unity method and Reference [41] where the method of directed graph is used to search the nodes at the quadrature points. The recursive procedure is as follows (to avoid confusing a *node* of the octree with a *node* \mathbf{x}_i used for the approximation, the latter is simply noted as \mathbf{x}_i in the rest of this subsection):

1. Build the top node of the tree that possesses a box (usually a cube) containing Ω and a list of pointers to all the \mathbf{x}_i . This is the current node.
2. If the current list possesses less pointers to \mathbf{x}_i than a fixed given number, or if the size of the current box is smaller than a fixed given size, this node is a final node at which the list of pointers is kept, go back to the upper level; otherwise:
 - (a) Create eight child nodes belonging to the current one. Divide the current box in eight and assign each to a child. Build the list for each child node by putting in it a pointer to the \mathbf{x}_i among the current list for which the domain of influence has a non-zero intersection with the box of the child node under consideration. Some \mathbf{x}_i are associated with several child nodes.
 - (b) Go to 2, the current node being the first of the child nodes.
 - (c) Once back here, do the same with the second, then the third and so on until the eighth node.
 - (d) Delete the list of pointers at the current node.
 - (e) Go back to the upper level or exit if this is the top node.

Now, given a point in Ω , we can quickly go down the tree from the top node to the final node, of which box the point stands in. It suffices to compare the coordinates of the point with the center of the current box in order to choose the appropriate child at each step. So we have a list of pointers to all the nodes that *may* influence the point. Now, we will just have to browse this list of candidate nodes to determine exactly the ones that *do* influence a given point. Without the octree, we would have to browse the entire list of nodes to determine those that influence this point.

If a node is added on a crack face, if a node is split into two or if an enriched node is added on a crack front, it is easily inserted at the top of the tree and moved down recursively to the final nodes of which box has a non-zero intersection with the domain of influence of this node.

We provide hereafter an illustration in two dimensions with the quadtree in Figure 13. 45 circular domains are in a square. For this example, we choose a limit of 25 \mathbf{x}_i for the stopping criteria. The big square is divided into four squares A, B, C and D. They are the child nodes of the big square. We loop on A, B, C and D and associate with them the domains among the 45 domains with which they have a non-zero intersection.

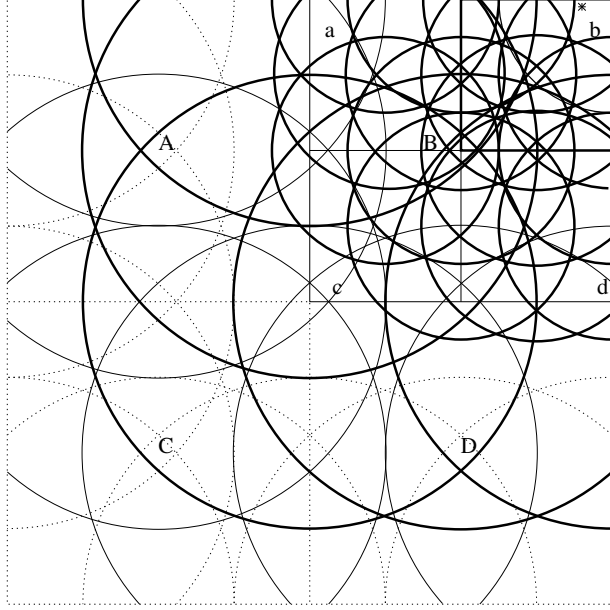


Figure 13: Example of a quadtree

There are 21 domains associated with A. We go down to A, observe that the stopping criteria is met and go up. There are 27 domains associated with B. These are plotted in straight line (bold or not). We go down to B and observe that the stopping criteria is not met. We divide B in four smaller squares (a, b, c, and d) and associate with each the domains among the 27 ones with which they have a non-zero intersection. The stopping criteria is met for each one. For example, 21 domains are associated with b, which are plotted in bold line. The domains list associated with B can be removed and we go one level up. Then, we associate 14 domains with C (stopping criteria met) and 21 with D (idem). The domains list associated with the big square can be removed. We go up one level and the algorithm ends. Now, if we search the non-zero weight functions at the point represented by the star in Figure 13, we quickly compare its coordinates with the center of the big square in the first step and with the center of B in the next step and conclude that the point belongs to b. So, we only compute the weight of the 21 \mathbf{x}_i associated with b instead of the 45 of the original set. The gain is of course highly more important in practice than on this simple example.

9.2 Efficient computation of $\phi_i(\mathbf{x})$ and $\phi_{i,k}(\mathbf{x})$

First, the expression in Equation (2) for the shape functions separates the factors $\mathbf{c}(\mathbf{x})$ depending on the current evaluation point, $\mathbf{p}(\mathbf{x}_i)$ depending on the node and $w_i(\mathbf{x})$ depending on both. To our knowledge, the shape functions were written that way for the first time in Reference [42]. This expression highlights the fact that it is more efficient to compute vector \mathbf{c} once for all nodes at a given point since it is the same for each node and then to loop on the nodes with a non-zero weight to compute the shape functions. This expression differs from the original one of Reference [1] that was re-used in Reference [2] and all the subsequent papers :

$$\phi_i(\mathbf{x}) = \sum_{j=1}^m p_j(\mathbf{x}) (\mathbf{A}^{-1}(\mathbf{x}) \mathbf{B}(\mathbf{x}))_{ji} \quad (42)$$

with

$$\mathbf{B}(\mathbf{x}) = [w_1(\mathbf{x}) \mathbf{p}(\mathbf{x}_1), w_1(\mathbf{x}) \mathbf{p}(\mathbf{x}_1), \dots, w_N(\mathbf{x}) \mathbf{p}(\mathbf{x}_N)] \quad (43)$$

that suggests performing a backward substitution for each node. Moreover, if the derivatives of the shape functions are to be computed, the derivation of Equation (2) shows that it is only necessary to compute the spatial derivatives $\mathbf{c}_{,k}$ (with $k = 1, 2, 3$) once for all nodes at a given point by re-using the factorization of the \mathbf{A} matrix and performing one backward substitution for each spatial derivative. They are indeed given by :

$$\phi_{i,k}(\mathbf{x}) = \mathbf{c}_{,k}^T(\mathbf{x}) \mathbf{p}(\mathbf{x}_i) w_i(\mathbf{x}) + \mathbf{c}^T(\mathbf{x}) \mathbf{p}(\mathbf{x}_i) w_{i,k}(\mathbf{x}) \quad (44)$$

with

$$\begin{aligned}
\mathbf{c}_{,k}(\mathbf{x}) &= (\mathbf{A}^{-1})_{,k}(\mathbf{x}) \mathbf{p}(\mathbf{x}) + \mathbf{A}^{-1}(\mathbf{x}) \mathbf{p}_{,k}(\mathbf{x}) \\
&= -\mathbf{A}^{-1}(\mathbf{x}) \mathbf{A}_{,k}(\mathbf{x}) \mathbf{A}^{-1}(\mathbf{x}) \mathbf{p}(\mathbf{x}) + \mathbf{A}^{-1}(\mathbf{x}) \mathbf{p}_{,k}(\mathbf{x}) \\
&= \mathbf{A}^{-1}(\mathbf{x}) [-\mathbf{A}_{,k}(\mathbf{x}) \mathbf{c}(\mathbf{x}) + \mathbf{p}_{,k}(\mathbf{x})] \\
&= \mathbf{A}^{-1}(\mathbf{x}) \mathbf{b}_k
\end{aligned} \tag{45}$$

and

$$\mathbf{A}_{,k}(\mathbf{x}) = \sum_{i=1}^{n^x} w_{i,k}(\mathbf{x}) \mathbf{p}(\mathbf{x}_i) \mathbf{p}^T(\mathbf{x}_i) \tag{46}$$

Second, we note that the dyadic products $\mathbf{p}(\mathbf{x}_i) \mathbf{p}^T(\mathbf{x}_i)$ in Equations (4) and (46) and the vectors $\mathbf{p}(\mathbf{x}_i)$ in Equations (2) and (44) do not depend on the evaluation point. So, if the size of the problem permits it, it is efficient to store once for all these values at each node, together with the coordinates of the node and a pointer to the weight function. Furthermore, we can benefit from the fact that the first basis function is always the unit function and that the next basis functions are the coordinates if the basis is at least linear. So, we can cleverly store only $\mathbf{p}(\mathbf{x}_i) \mathbf{p}^T(\mathbf{x}_i)$ and find inside it the basis $\mathbf{p}(\mathbf{x}_i)$ and the coordinates \mathbf{x}_i . For example, for a linear basis, the dyadic product is

$$\mathbf{p}(\mathbf{x}_i) \mathbf{p}^T(\mathbf{x}_i) = \begin{pmatrix} 1 & x_i & y_i & z_i \\ x_i & x_i^2 & x_i y_i & x_i z_i \\ y_i & x_i y_i & y_i^2 & y_i z_i \\ z_i & x_i z_i & y_i z_i & z_i^2 \end{pmatrix} \tag{47}$$

and it suffices to store the lower part of this symmetric matrix in the following array

$$\boxed{\boxed{1 \quad \boxed{x_i \quad y_i \quad z_i} \quad x_i^2 \quad x_i y_i \quad x_i z_i \quad y_i^2 \quad y_i z_i \quad z_i^2}}$$

and to return the array of elements 2, 3 and 4 to get the coordinates and the array of elements 1, 2, 3 and 4 to get the basis.

Finally, after these preliminary steps, the algorithm to compute ϕ_i and $\phi_{i,k}$ for every given \mathbf{x} is as follows:

1. Find the list of candidate nodes with the help of the tree.
2. Loop on the candidate nodes and compute the weight function. Depending on the type of the node, this can be a normal weight, a normal weight modified by the diffraction criterion or an enriched weight. If the weight function of the candidate is non-zero, it is an influencing node; so:
 - (a) store the weight and its derivatives,
 - (b) add the contribution of this candidate to \mathbf{A} by Equation (4) and $\mathbf{A}_{,k}$ by Equation (46) for $k = 1, 2, 3$ with the help of the pre-computed dyadic products.
3. Compute the Cholesky factorization of \mathbf{A} . We can use the computationally more efficient Cholesky factorization instead of the LU factorization since \mathbf{A} is symmetric definite positive.
4. Compute \mathbf{p} and then \mathbf{c} by Equation (3) with the help of the factorization of \mathbf{A} .
5. For $k = 1, 2, 3$, compute $\mathbf{p}_{,k}$, then $\mathbf{b}_k = \mathbf{p}_{,k}(\mathbf{x}) - \mathbf{A}_{,k}(\mathbf{x}) \mathbf{c}(\mathbf{x})$ and finally $\mathbf{c}_{,k}$ by Equation (45) with the help of the factorization of \mathbf{A} .
6. Loop on all the influencing nodes ($i = 1, 2, \dots, n^x$):
 - (a) Compute $\mathbf{c}^T(\mathbf{x}) \mathbf{p}(\mathbf{x}_i)$ with the help of the pre-computed $\mathbf{p}(\mathbf{x}_i)$,
 - (b) Compute ϕ_i by Equation (2) knowing $\mathbf{c}^T(\mathbf{x}) \mathbf{p}(\mathbf{x}_i)$ and the stored $w_i(\mathbf{x})$.
 - (c) For $k = 1, 2, 3$, compute $\phi_{i,k}$ by (44) knowing $\mathbf{c}^T(\mathbf{x}) \mathbf{p}(\mathbf{x}_i)$, $\mathbf{c}_{,k}$, the pre-computed $\mathbf{p}(\mathbf{x}_i)$ and the stored $w_i(\mathbf{x})$ and $w_{i,k}(\mathbf{x})$.

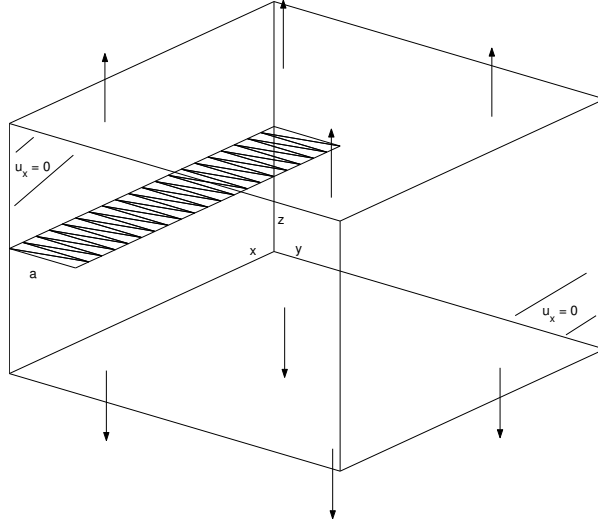


Figure 14: Plane crack under tension in a cube

10 NUMERICAL RESULTS

In the following numerical results, we study a cracked cube under various configurations. The shape, size and number of the cracks as well as the boundary conditions change from one example to another. We always use a regular distribution of $21 \times 21 \times 21$ nodes. We perform the volume integration on $20 \times 20 \times 20$ cells with $8 \times 8 \times 8$ Gauss points. The integrations on the surfaces for the boundary conditions are performed on 20×20 cells with 8×8 Gauss points. We use academic material properties: $E = 1$ and $\nu = 0.3$. The side of the cube is $2W = 2$.

10.1 Plane crack under tension

The first example is in fact the three-dimensional version of a two-dimensional plane-strain edge-cracked square under tension that was solved in Section 5.2 of Reference [29]. The cube shown in Figure 14 has a plane crack of length a in its face $y = -1$. The normal displacement on the faces $x = \pm 1$ is fixed to zero in order to reproduce plane strain conditions. The traction on the faces $z = \pm 1$ is $\sigma = 1$. The crack is modeled with 40 triangles and the crack length vary from 0.2 to 1.6 with step of 0.2. Some nodes are located on the crack and are split into two. The problem is solved without enriched nodes on one hand and with 21 triplets of enriched nodes, that are located on the triangles vertices on the front. The support radius of each node (either normal or enriched) is 0.14. The stress intensity factors are computed on 19 cubes with a side of 0.2 that are centered on the triangles vertices on the front except those on a face $x = \pm 1$.

This problem has a known solution: K_I is constant along the front and is equal to:

$$K_I = F_I(\alpha)\sigma\sqrt{\pi a} \quad (48)$$

with $\alpha = \frac{a}{W}$. The shape factor F_I is the same than in two dimensions and can be found in Reference [43]. The numerical solution with both methods along the front for $a = 1.6$ is shown in Figure 15. We observe that the stress intensity factor is nearly constant along the front and that the enriched method gives a closer result to the reference. The mean F_I is given in Table 1 for the various length and plotted in Figure 16. We observe a significant improvement of the results thanks to the enriched nodes. For small values of a , the error is more than 5% for the non-enriched method and less than 1% for the enriched one. For $a = 0.4$ and $a = 0.6$, the difference between the result of the enriched method and the reference value is even lower than the reference accuracy. The computational overhead of the enriched method is only about 15% of the CPU cost of the non-enriched method.

10.2 Penny-shaped crack under tension

A penny-shaped crack of radius a varying from 0.1 to 0.7 is in a cube under a tension $\sigma_z = 1$. The crack is modeled with 16 triangles (see Figure 17). The problem is solved without enriched nodes on one hand and

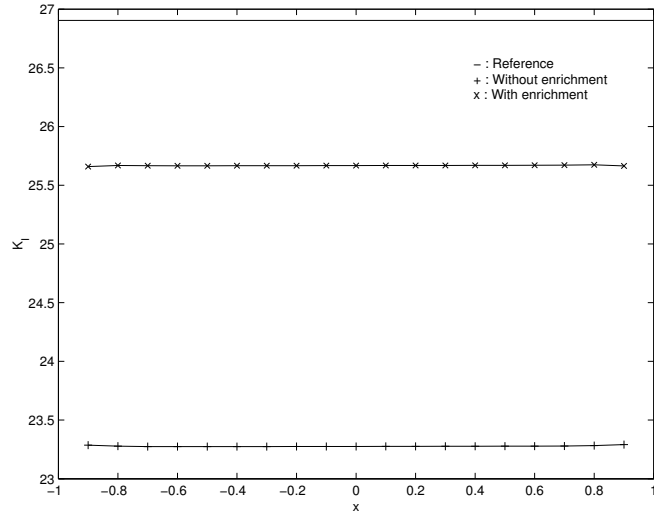


Figure 15: Mode I stress intensity factor for the plane crack under tension ($a = 1.6$)

Crack length	0.2	0.4	0.6	0.8	1.0	1.2	1.4	1.6
F_I Reference [43]	1.23	1.49	1.85	2.32	3.01	4.15	6.40	12.0
F_I non-enriched	1.157	1.398	1.733	2.174	2.799	3.812	5.759	10.383
Error non-enriched	5.9%	6.2%	6.3%	6.3%	7.0%	8.1%	10.0%	13.5%
F_I enriched	1.224	1.490	1.852	2.327	3.002	4.108	6.255	11.449
Error enriched	0.51%	0.03%	0.09%	0.30%	0.25%	1.0%	2.3%	4.6%

Table 1: Normalized stress intensity factor for the plane crack under tension

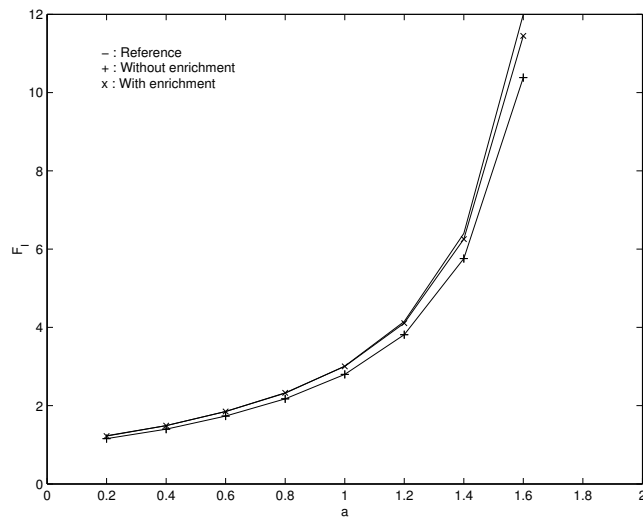


Figure 16: Normalized stress intensity factor for the plane crack under tension

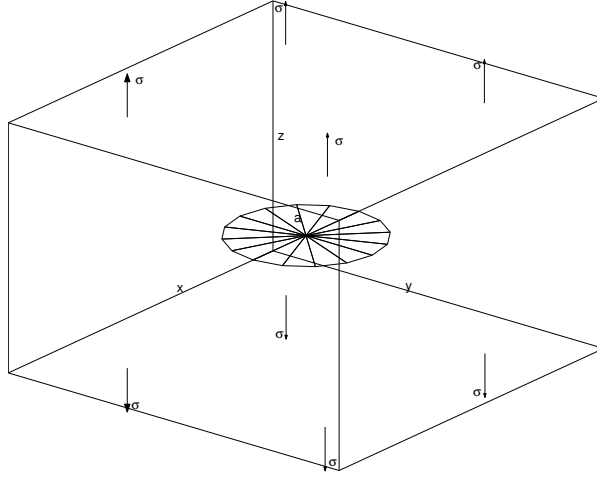


Figure 17: Penny-shaped crack in a cube under tension

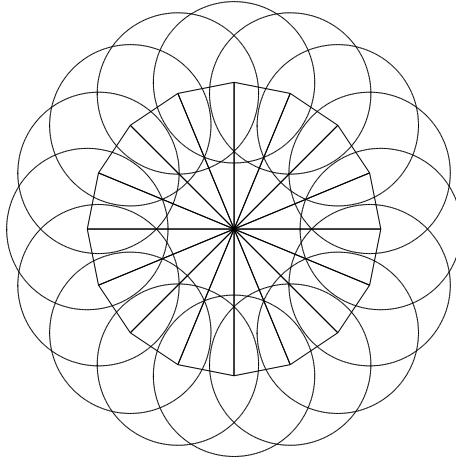


Figure 18: Enriched nodes supports

with 21 triplets of enriched nodes. Contrary to the previous example, the radius of the enriched spherical domains increases with the radius of the crack in order to always have an overlap of the enriched domains. We take $R_{enr} = 1.4 \times \frac{2\pi}{16} \times a$, that is 1.4 times the distance between two neighboring enriched nodes. These enriched supports are shown in two dimensions in the plane of the crack in Figure 18. The stress intensity factors are computed on the 16 same points where the enriched nodes are located.

The solution of this problem is

$$K_I = F_I(\alpha, \theta) 2\sigma \sqrt{\frac{a}{\pi}} \quad (49)$$

where $\alpha = \frac{a}{W}$ and θ is the angle along the front. If the radius of the crack is negligible with respect to the side of the cube, the shape factor does not depend on θ and is equal to 1. But, we do not make this assumption. The mean normalized stress intensity factor is presented in Table 2. We observe that it is close to 1 if a is small with respect to W for both methods. The values for the enriched method are 3 or 4% superior with respect to the non-enriched method as it was always the case in the previous example and in all the examples in Reference [29]. This suggests that the enriched method again improves the solution but we can not be sure since we do not have a reference solution when the assumption that the radius of the crack is negligible with respect to the side of the cube is not made. So, we also present in Table 2 and Figure 19 the value of minus the total energy $-E_T$ of the numerical solutions. A greater value indicates a better solution (see on this subject Reference [44] for the application of this energy criterion and a conjugated energy criterion with a meshless method). So, we can conclude that the enriched method gives a better solution.

Crack radius		0.1	0.2	0.3	0.4	0.5	0.6	0.7
F_I	non-enriched	1.0036	1.0044	1.0207	1.0251	1.0518	1.1059	1.1770
$-E_T$	non-enriched	4.00126	4.01351	4.05323	4.13555	4.28557	4.53572	4.93374
F_I	enriched	1.0287	1.0422	1.0516	1.0522	1.0859	1.1354	1.2100
$-E_T$	enriched	4.00149	4.01584	4.05841	4.14514	4.30116	4.55736	4.96788

Table 2: Normalized stress intensity factors and energy for the penny-shaped crack under tension

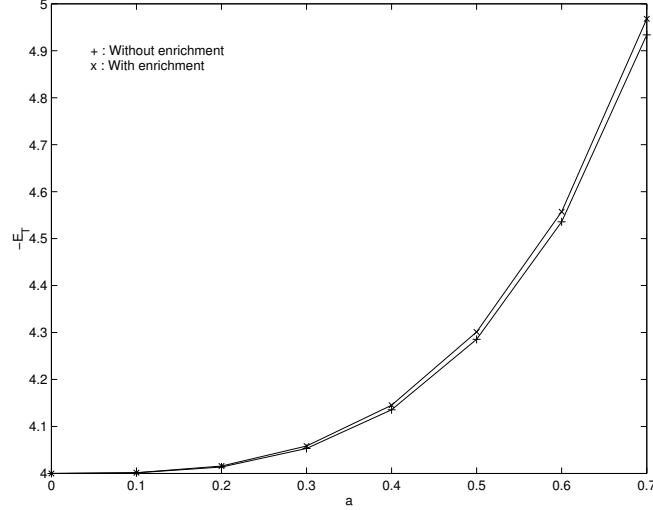


Figure 19: Energy for the penny-shaped crack under tension

10.3 Penny-shaped crack under shear

To validate the method in mixed-mode, we submit the cube with a penny-shaped crack to a shear $\tau_{xz} = 1$ on the planes $x = \pm 1$ and $z = \pm 1$ (see Figure 20). The solution is

$$K_I = 0 \quad (50)$$

$$K_{II} = -F_{II}(\alpha, \theta)\tau\sqrt{\pi a} \cos \theta \quad (51)$$

$$K_{III} = F_{III}(\alpha, \theta)\tau\sqrt{\pi a} \sin \theta \quad (52)$$

where $\alpha = \frac{a}{W}$ and θ is measured from the x axis. If $\alpha \rightarrow 0$, the shape factors do not depend on θ and $F_{II} \rightarrow 0.7490$ and $F_{III} \rightarrow 0.5243$. But again, we do not make this assumption.

The stress intensity factors along the crack for mode II and mode III for a radius varying from 0.1 to 0.7 by step of 0.1 are shown in Figure 21. We can qualitatively validate the results since K_{II} is about proportional to $-\cos \theta$ and K_{III} to $\sin \theta$. Moreover, the ratio between the stress intensity factors of the modes II and III is about the same than the ratio between those of the reference. As before, the stress intensity factors for the enriched method are superior to those of the non-enriched method. To ensure that the enriched method gives indeed better results, we present the total energy in Table 3 and Figure 22. The value of $-E_T$ is always superior for the enriched method and we can conclude that the enrichment also improves the solution in mixed-mode.

Crack radius		0.1	0.2	0.3	0.4	0.5	0.6	0.7
$-E_T$	non-enriched	10.4012	10.4146	10.4590	10.5503	10.7145	10.9815	11.3932
$-E_T$	enriched	10.4016	10.4188	10.4690	10.5698	10.7442	11.0206	11.4548

Table 3: Energy for the penny-shaped crack under shear

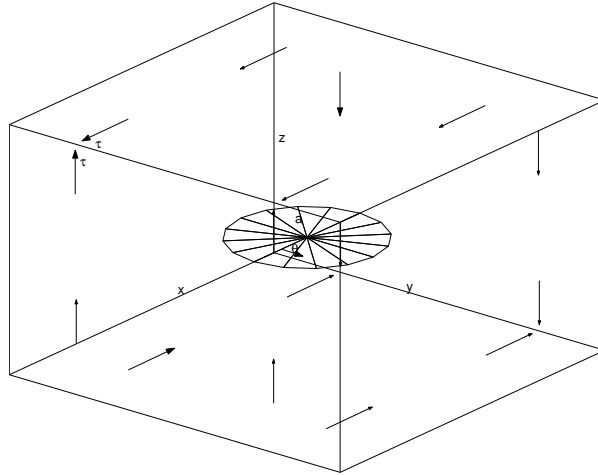


Figure 20: Penny-shaped crack in a cube under shear

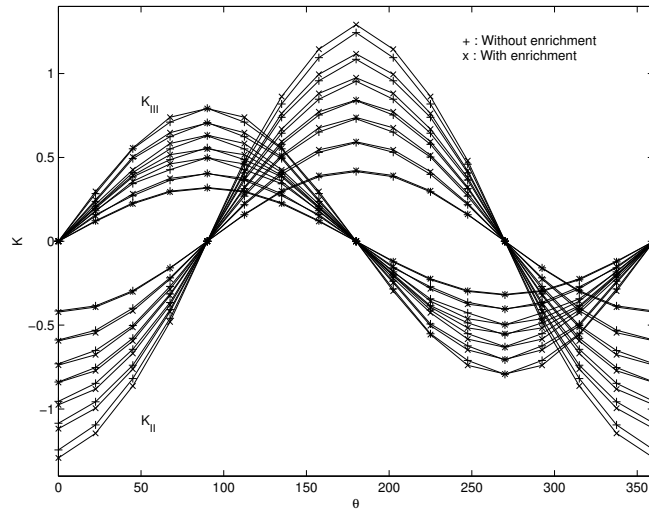


Figure 21: Stress intensity factors for the penny-shaped crack under shear (a vary from 0.1 to 0.7)

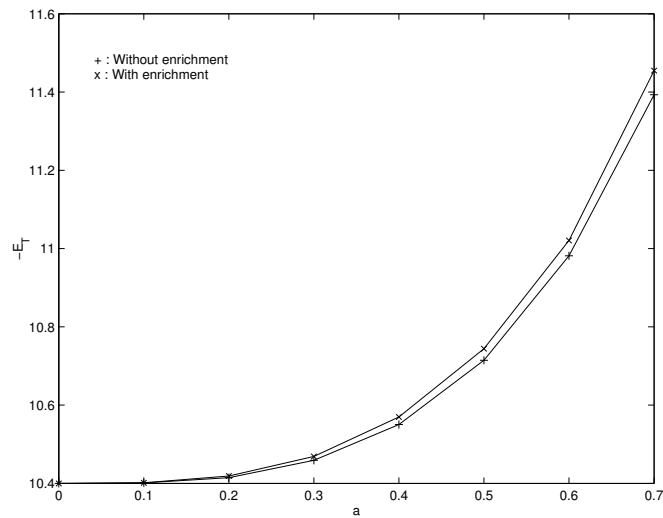


Figure 22: Energy for the penny-shaped crack under shear

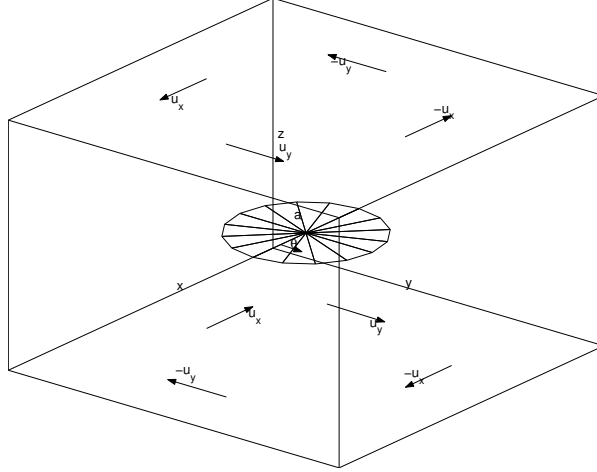


Figure 23: Penny-shaped crack in a cube under torsion

Crack radius	0.1	0.2	0.3	0.4	0.5	0.6	0.7
$-E_T$ non-enriched	-0.866464	-0.866440	-0.866237	-0.865415	-0.863084	-0.857699	-0.847059
$-E_T$ enriched	-0.866463	-0.866429	-0.866176	-0.865245	-0.862693	-0.857077	-0.845994

Table 4: Energy for the penny-shaped crack under torsion

10.4 Penny-shaped crack under torsion

For the last example of a non-propagating crack, we submit the cube to torsion. The displacement is enforced on the faces $z = \pm 1$ (see Figure 23):

$$u_x = \gamma y z \quad (53)$$

$$u_y = -\gamma x z \quad (54)$$

We take the academic value $\gamma = 1$. This is a pure tearing problem.

Mode III stress intensity factors are plotted on Figure 24 for seven crack radii. It is greater in absolute value in $\theta = k \times 90^\circ$ than in $\theta = (2k + 1) \times 45^\circ$ (k integer). This is due to the fact that for a fixed distance to the center in a square cross section of the bar, the torsion stress is more important near the boundary. The reference for this kind of problem is the crack in a infinite medium submitted to a torsion couple M_T for which

$$K_{III} = \frac{8M_T}{3\pi^{\frac{3}{2}} a^{\frac{5}{2}}} \quad (55)$$

We could integrate the reaction on the faces where the displacement is enforced in order to obtain the torsion couple but this reference would not be very useful since we can still not make the assumption that the crack is in an infinite medium. We observe that the increase in K_{III} between the non-enriched and the enriched method is not as important than in the previous cases. The value of $-E_T$ is given in Table 4 and plotted in Figure 25. It is again superior for the enriched method for each crack radius. However, we observe that the relative difference in energy is inferior than in the previous cases. These two observations seem to indicate that the enrichment does not improve the results as much for problems dominated by mode III.

10.5 Inclined penny-shaped crack under tension

A penny-shaped crack of radius $a = 0.2$, that makes an angle $\beta = 30^\circ$ with the x axis, is in a cube under a tension $\sigma = 1$ (see Figure 26). First, we examine the value of the stress intensity factors as a function of the angle θ obtained by the non-enriched and the enriched methods. Next, we compute the propagation of the crack by the latter method.

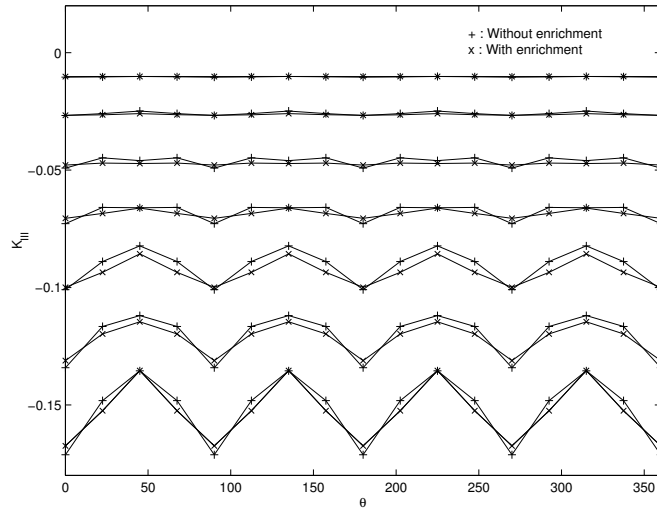


Figure 24: Stress intensity factors for the penny-shaped crack under torsion

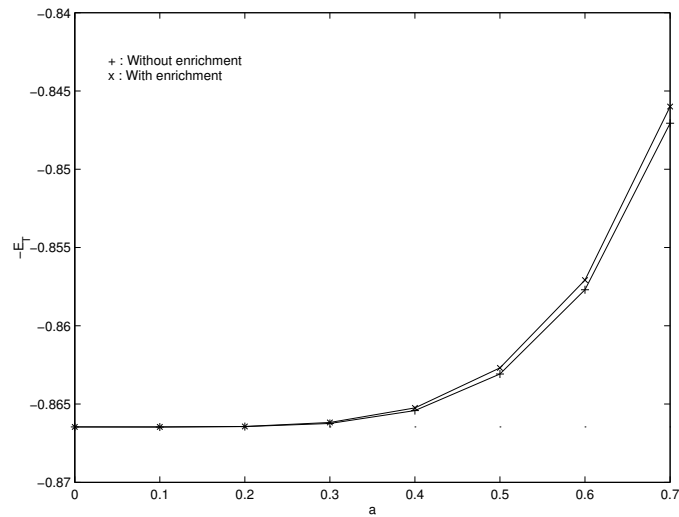


Figure 25: Energy for the penny-shaped crack under torsion

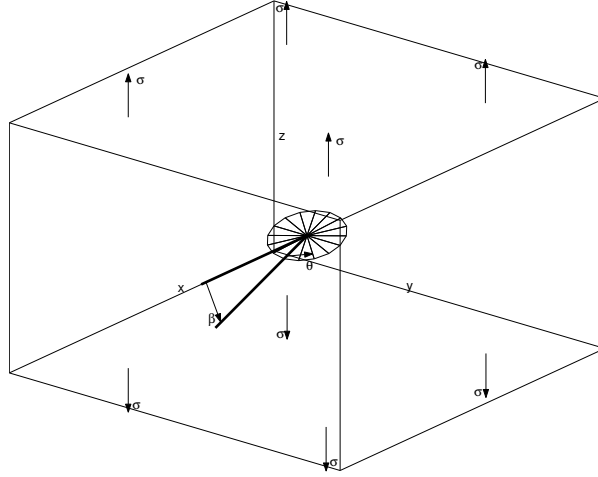


Figure 26: Inclined penny-shaped crack in a cube under tension

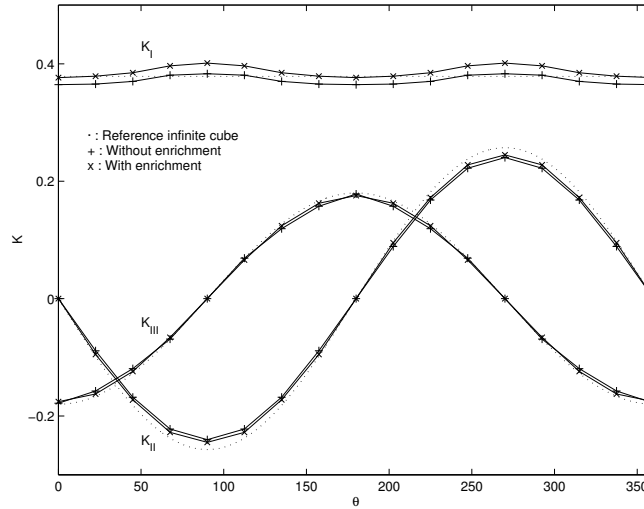


Figure 27: Stress intensity factors for the inclined crack

If the size of the crack is negligible with respect to the size of the cube, the solution is as follows:

$$K_I = 2\sigma \cos^2 \beta \sqrt{\frac{a}{\pi}} \quad (56)$$

$$K_{II} = -\frac{4\sigma}{2-\nu} \sin \beta \cos \beta \sqrt{\frac{a}{\pi}} \sin \theta \quad (57)$$

$$K_{III} = -\frac{4(1-\nu)\sigma}{2-\nu} \sin \beta \cos \beta \sqrt{\frac{a}{\pi}} \cos \theta \quad (58)$$

The results are plotted in Figure 27 together with this reference. Once again, the enriched method gives superior stress intensity factors. The reference value in an infinite medium for the mode I stress intensity factor is closer to the result of the non-enriched method than to the one of the enriched method. But, if we knew the exact value of the shape factor that slightly increases the stress intensity factor, we are convinced that the reference would be closer to the latter. Indeed, the value of $-E_T$ for the non-enriched method (4.01004) is inferior to the enriched method (4.01214). The latter is thus the one that gives the best result. So, this is the method we use for the propagation simulation.

A cyclic loading from $\sigma_{\min} = 0$ to $\sigma_{\max} = 1$ is applied and the crack propagates in fatigue. The maximum step is taken as 0.1 and we let the crack grows until it reaches a boundary. The 16 triplets of enriched nodes move when the crack grows and the radius of their influence domains increases in order to maintain an overlap of the enriched domains. The nine steps of the propagation are shown in Figure 28 and the last step is shown

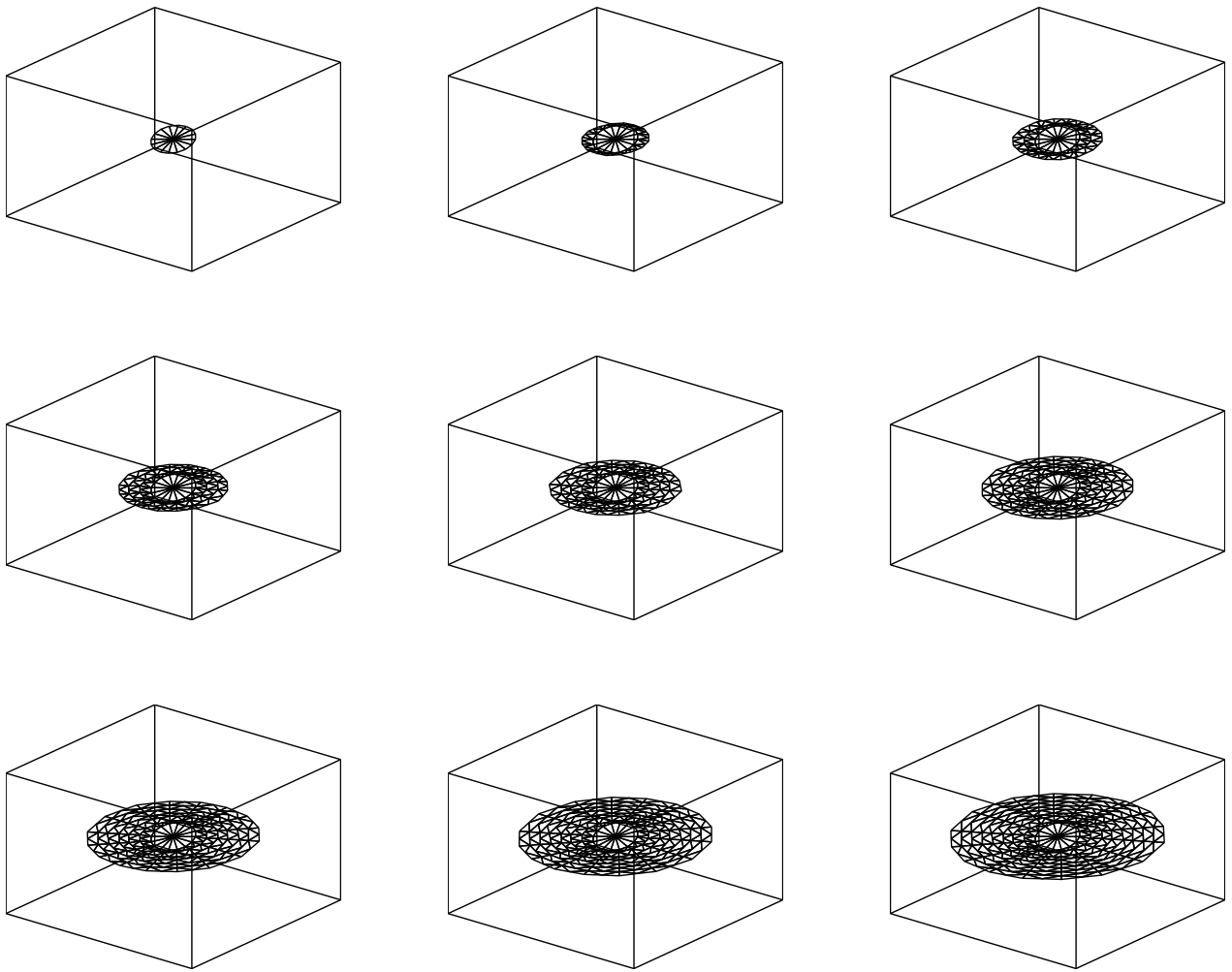


Figure 28: Nine steps of the propagation of the inclined crack

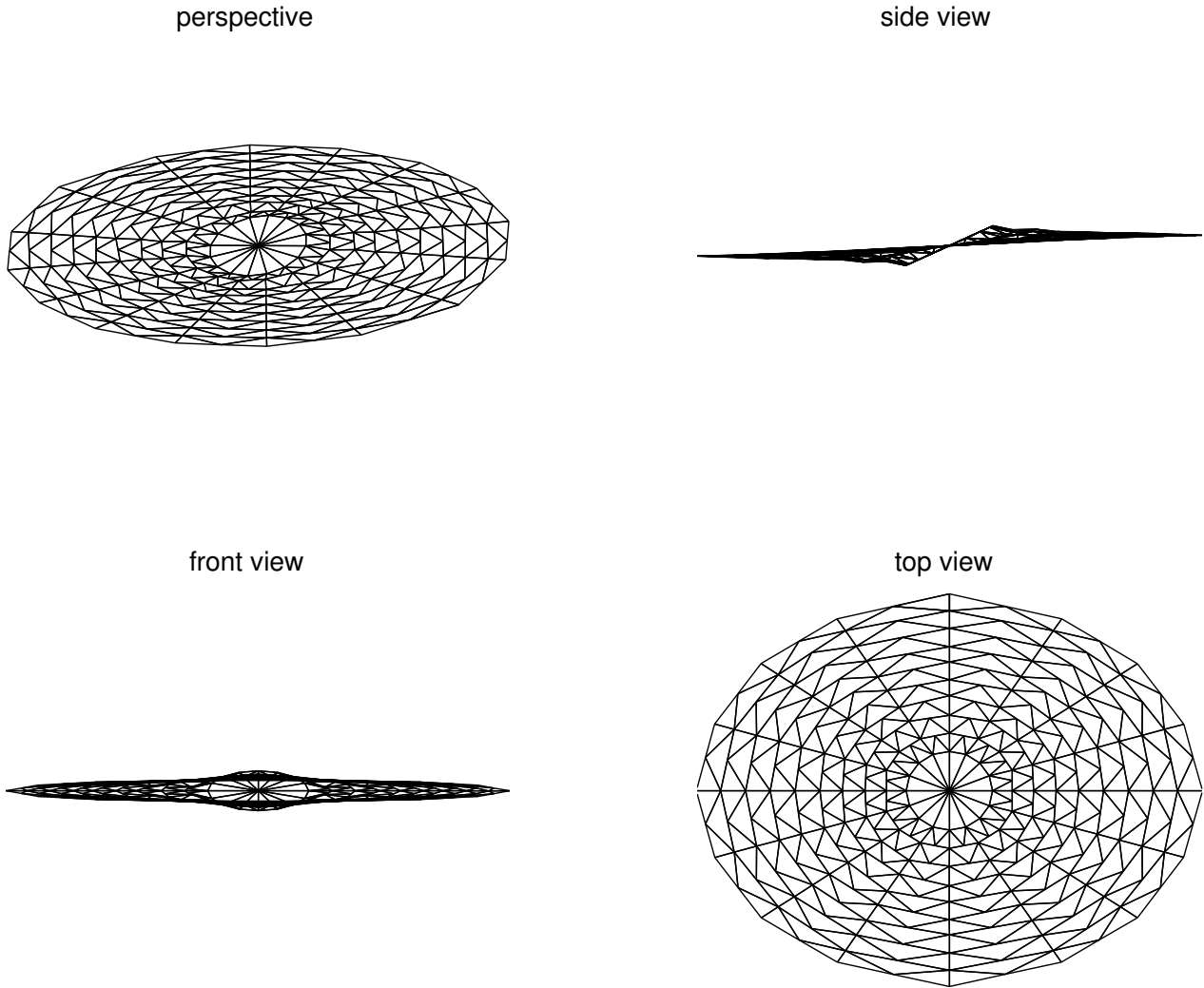


Figure 29: Inclined crack after propagation

from different points of view in Figure 29. The second step is actually the crack that is used in the figures in Sections 3 to 8. At the end of the propagation, 448 triangles model the crack. The result is in good agreement with those obtained by a non-enriched meshless method coupled to the finite element method in Reference [32] and by the extended finite element method in Reference [5]. We observe that the crack tends to stay more or less circular and to align itself in a normal plane to the tension direction. This is similar to the behavior of the inclined crack in two dimensions in Section 5.4 of Reference [29].

10.6 A pair of penny-shaped cracks under tension

The last example still uses the same cube under cyclic tension but there are more than one crack and we study their interaction during the propagation. Two parallel, non-coplanar and non-aligned cracks with radius $a = 0.1$ and normal parallel to the tension direction are in the cube (Figure 30). The spacing Δz between their centers in the direction of the traction is 0.2 and the spacing Δx in a perpendicular direction is 0.4.

Six steps of the propagation are shown in Figure 31. The last position is detailed in Figure 32. 512 triangles are necessary to represent the pair of cracks at the last step. At the beginning of the propagation, both cracks grow in their plane but when there is an overlap between the crack, they warp and grow toward the other. When the overlap is important, the stress intensity factors decrease in the part of the front where there is overlap and the cracks continue to grow toward the external boundary. The side view in Figure 32 is similar to the two-dimensional propagation of the pair of cracks in Section 5.5 of Reference [29]. Our result is in agreement with the result of Reference [45] obtained by the boundary element method with different dimensions.

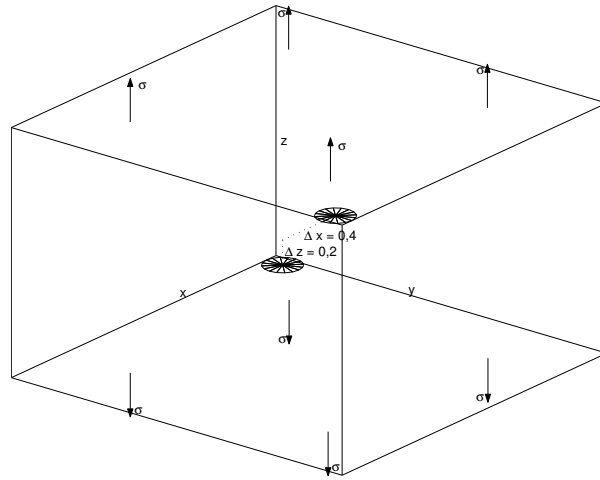


Figure 30: Pair of crack in a cube under tension

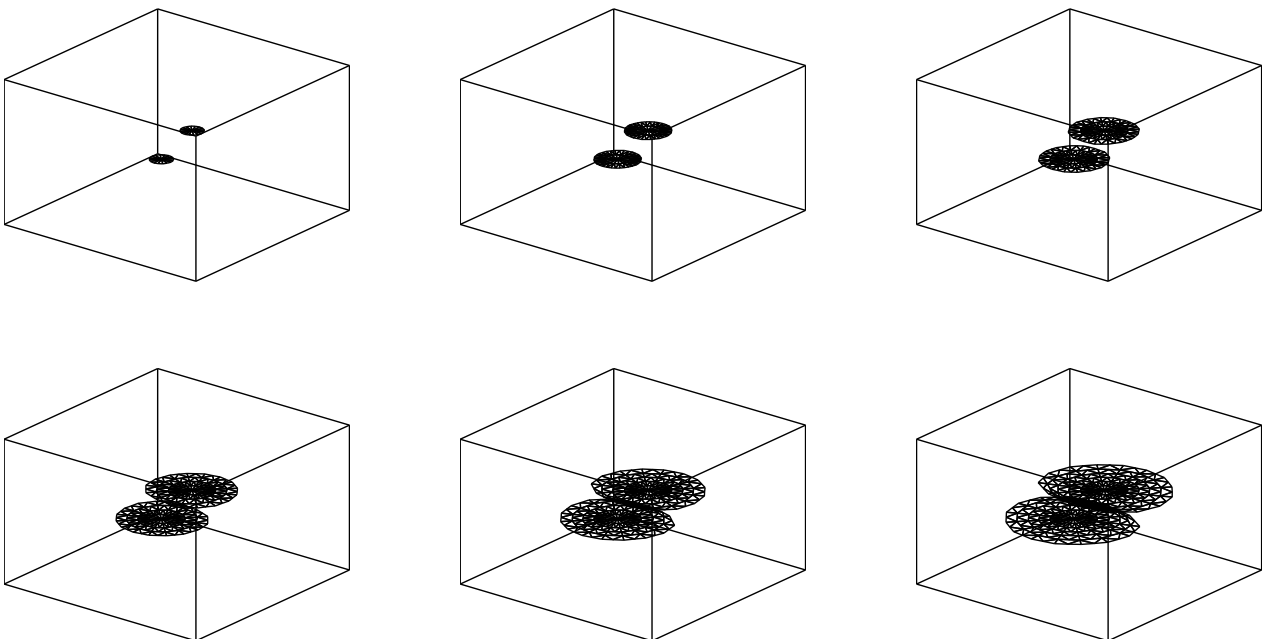
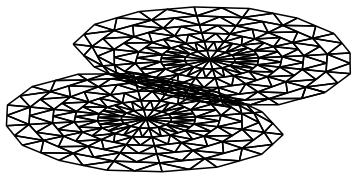


Figure 31: Six steps of the propagation of the pair of cracks

perspective



side view



front view



top view

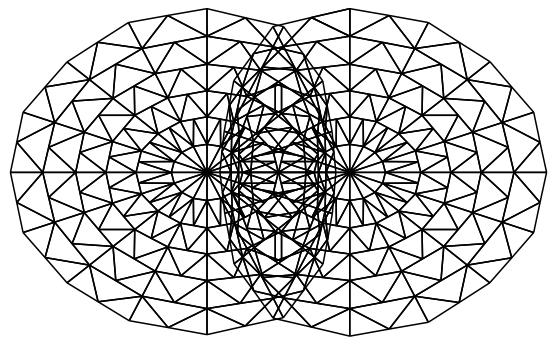


Figure 32: Pair of crack after propagation

11 CONCLUSIONS

As in two dimensions, the enrichment technique of the shape functions space by means of some special weight functions proves to be simple and efficient to get an approximation of the displacement field of good quality in the vicinity of the crack front. A significant improvement of the solution is obtained for a low computational overhead. Thanks to this enrichment, a relatively coarse nodal distribution can be used inside which the crack propagate with a kind of enriched tubular region moving with the crack front. The enriched method is able to simulate complex crack propagation even if the points of the front propagate at different rates in different directions in such a way that the crack wraps like in the last example of the pair of cracks propagating toward each other. The simulation of the propagation of the pair of cracks by a conventional finite element method would require an important user intervention for remeshing while it is fully automatic with the enriched meshless method.

We contemplate several improvements of the method described in this paper. First, the stress intensity factors computation explained in Section 7 is a simple extension of the two-dimensional theory that takes into account neither the curvature of the front nor the wrapping of the crack. Two ways to take them into account is the application of the theory of Reference [46] or the use of a virtual velocity extension field \mathbf{q} tangent to the crack faces instead of a scalar weight q in Equations (33) to (35) by the technique that was developed in the framework of the extended finite element method in Reference [4].

Second, the crack representation by a set of triangles does not permit us to easily treat edge cracks or changes in the topology when the crack reaches a boundary. A combination of the enriched method with a level set representation of the crack is an interesting perspective of this work

Third, the method could be further optimized. In two dimensions, the propagation results that we obtained in Reference [29] took typically less than one minute (on a 2.8 GHz Xeon personal computer). But, even with the efficient algorithms that were presented, the problem of the pair of cracks in three dimensions for example takes up to five hours. Some ideas to decrease this computational time are the following:

- an algorithm that determines the region affected by the crack propagation in order to modify the contribution of this region to the stiffness matrix instead of recomputing the full stiffness matrix at each step of the propagation,
- an irregular distribution of the nodes,
- a decrease in the number of integration points in the cells that are not cut by the crack,
- either a more efficient algorithm for the diffraction criteria that does not check every triangle for every node, because this algorithm takes a significant part of the computational time when there are hundreds of triangles, or a level set representation of the crack to speed up the diffraction criterion.

ACKNOWLEDGMENTS

This work was realized in the university of Liège and was partly financially supported by the Belgian National Fund for Scientific Research (F.N.R.S.).

REFERENCES

- [1] B. Nayroles, G. Touzot, and P. Villon. Generalizing the finite element method: Diffuse approximation and diffuse elements. *Computational Mechanics*, 10:307–318, 1992.
- [2] T. Belytschko, Y. Y. Lu, and L. Gu. Element-free Galerkin methods. *International Journal for Numerical Methods in Engineering*, 37:229–256, 1994.
- [3] Y. Mi and M. H. Aliabadi. Three-dimensional crack growth simulation using BEM. *Computers and Structures*, 52:871–878, 1993.
- [4] N. Moës, A. Gravouil, and T. Belytschko. Non-planar 3d crack growth by the extended finite element and level sets—part I: Mechanical model. *International Journal for Numerical Methods in Engineering*, 53:2549–2568, 2002.

- [5] A. Gravouil, N. Moës, and T. Belytschko. Non-planar 3d crack growth by the extended finite element and level sets—part II: Level set update. *International Journal for Numerical Methods in Engineering*, 53:2569–2586, 2002.
- [6] T. Belytschko, L. Gu, and Y. Y. Lu. Fracture and crack growth by element-free Galerkin methods. *Modelling and Simulation in Materials Science and Engineering*, 2:519–534, 1994.
- [7] T. Belytschko, Y. Y. Lu, and L. Gu. Crack propagation by element-free Galerkin methods. *Engineering Fracture Mechanics*, 51(2):295–315, 1995.
- [8] T. Belytschko, Y. Y. Lu, L. Gu, and M. Tabbara. Element-free Galerkin methods for static and dynamic fracture. *International Journal of Solids and Structures*, 32(17–18):2547–2570, 1995.
- [9] Y. Y. Lu, T. Belytschko, and M. Tabbara. Element-free Galerkin method for wave propagation and dynamic fracture. *Computer Methods in Applied Mechanics and Engineering*, 126:131–153, 1995.
- [10] T. Belytschko and M. Tabbara. Dynamic fracture using element-free Galerkin methods. *International Journal for Numerical Methods in Engineering*, 39:923–938, 1996.
- [11] T. Belytschko, D. Organ, and Y. Krongauz. A coupled finite element–element-free Galerkin method. *Computational Mechanics*, 17:186–195, 1996.
- [12] D. Organ, M. Fleming, T. Terry, and T. Belytschko. Continuous meshless approximations for nonconvex bodies by diffraction and transparency. *Computational Mechanics*, 18:1–11, 1996.
- [13] T. Belytschko, Y. Krongauz, D. Organ, M. Fleming, and P. Krysl. Meshless methods: An overview and recent developments. *Computer Methods in Applied Mechanics and Engineering*, 139:3–47, 1996.
- [14] M. Fleming, Y. A. Chu, B. Moran, and T. Belytschko. Enriched element-free Galerkin methods for crack tip fields. *International Journal for Numerical Methods in Engineering*, 40:1483–1504, 1997.
- [15] J.-P. Ponthot and T. Belytschko. Arbitrary lagrangian-eulerian formulation for element-free Galerkin method. *Computer Methods in Applied Mechanics and Engineering*, 152:19–46, 1998.
- [16] T. Belytschko, D. Organ, and C. Gerlach. Element-free Galerkin methods for dynamic fracture in concrete. *Computer Methods in Applied Mechanics and Engineering*, 187:385–399, 2000.
- [17] G. Ventura, J. X. Xu, and T. Belytschko. A vector level set method and new discontinuity approximations for crack growth by EFG. *International Journal for Numerical Methods in Engineering*, 54:923–944, 2002.
- [18] M. R. Tabbara and C. M. Stone. A computational method for quasi-static fracture. *Computational Mechanics*, 22:203–210, 1998.
- [19] Y. Xu and S. Saigal. An element free Galerkin method for stable crack growth in an elastic solid. *Computer Methods in Applied Mechanics and Engineering*, 154:331–343, 1998.
- [20] Y. Xu and S. Saigal. Element free Galerkin study of steady quasi-static crack growth in plane strain tension in elastic-plastic materials. *Computational Mechanics*, 22:255–265, 1998.
- [21] B. N. Rao and S. Rahman. An efficient meshless method for fracture analysis of cracks. *Computational Mechanics*, 26:398–408, 2000.
- [22] B. N. Rao and S. Rahman. A coupled meshless-finite element method for fracture analysis of cracks. *International Journal of Pressure Vessels and Piping*, 78:647–657, 2001.
- [23] B. N. Rao and S. Rahman. Probabilistic fracture mechanics by Galerkin meshless methods—Part I: Rates of stress intensity factors. *Computational Mechanics*, 28:351–364, 2002.
- [24] B. N. Rao and S. Rahman. Probabilistic fracture mechanics by Galerkin meshless methods—Part II: Reliability analysis. *Computational Mechanics*, 28:365–374, 2002.
- [25] B. N. Rao and S. Rahman. An enriched meshless method for non-linear fracture mechanics. *International Journal for Numerical Methods in Engineering*, 59:197–223, 2004.

- [26] H. Karutz, R. Chudoba, and W. B. Krätzig. Automatic adaptive generation of a coupled finite element/element-free Galerkin discretization. *Finite Elements in Analysis and Design*, 38:1075–1091, 2002.
- [27] G. H. Lee, H. J. Chung, and C. K. Choi. Adaptive crack propagation analysis with the element-free Galerkin method. *International Journal for Numerical Methods in Engineering*, 56:331–350, 2003.
- [28] S. H. Lee and Y. C. Yoon. An improved crack analysis technique by element-free Galerkin method with auxiliary supports. *International Journal for Numerical Methods in Engineering*, 56:1291–1314, 2003.
- [29] M. Duflot and H. Nguyen-Dang. A meshless method with enriched weight functions for fatigue crack growth. *International Journal for Numerical Methods in Engineering*, 59:1945–1961, 2004.
- [30] Y. Chen, A. Eskandarian, M. Oskard, and J. D. Lee. Meshless analysis of plasticity with application to crack growth problems. *Theoretical and Applied Fracture Mechanics*, 41:83–94, 2004.
- [31] N. Sukumar, B. Moran, T. Black, and T. Belytschko. An element-free Galerkin method for three-dimensional fracture mechanics. *Computational Mechanics*, 20:170–175, 1997.
- [32] P. Krysl and T. Belytschko. The element-free Galerkin method for dynamic propagation of arbitrary 3-D cracks. *International Journal for Numerical Methods in Engineering*, 44:767–800, 1999.
- [33] D. Hegen. *An Element-Free Galerkin Method for Crack Propagation in Brittle Materials*. PhD thesis, Technische Universiteit Eindhoven, March 1997.
- [34] A. Carpinteri, G. Ferro, and G. Ventura. An augmented Lagrangian element free (ALEF) approach for crack discontinuities. *Computer Methods in Applied Mechanics and Engineering*, 191:941–957, 2001.
- [35] P. Krysl and T. Belytschko. Element-free Galerkin method: Convergence of the continuous and discontinuous shape functions. *Computer Methods in Applied Mechanics and Engineering*, 148:257–277, 1997.
- [36] M. Fleming. *Element-Free Galerkin Method for Fatigue and Quasi-Static Fracture*. PhD thesis, Northwestern University, June 1997.
- [37] J. F. Yau, S. S. Wang, and H. T. Corten. A mixed-mode crack analysis of isotropic solids using conservation laws of elasticity. *Journal of Applied Mechanics*, 47:335–341, 1980.
- [38] B. Moran and C. F. Shih. Crack tip and associated domain integrals from momentum and energy balance. *Engineering Fracture Mechanics*, 27(6):615–641, 1987.
- [39] H. A. Richard, M. Fulland, and M. Sander. Theoretical crack path prediction. *Fatigue and Fracture of Engineering Materials and Structures*, 28:3–12, 2005.
- [40] O. Klaas and M. S. Shepard. Automatic generation of octree-based three-dimensional discretizations for partition of unity methods. *Computational Mechanics*, 25:296–304, 2000.
- [41] S. Hagihara, M. Tsunori, T. Ikeda, and N. Miyazaki. Element-free Galerkin method using directed graph and its application to creep problems. *Computational Mechanics*, 31:489–495, 2003.
- [42] M. Duflot and H. Nguyen-Dang. A truly meshless method based on a moving least squares quadrature. *Communications in Numerical Methods in Engineering*, 18:441–449, 2002.
- [43] Y. Murakami, editor. *Stress Intensity Factors Handbook*. Pergamon Press, Oxford, 1987.
- [44] M. Duflot and H. Nguyen-Dang. Dual analysis by a meshless method. *Communications in Numerical Methods in Engineering*, 18:621–631, 2002.
- [45] P. Partheymüller, M. Haas, and G. Kuhn. Comparison of the basic and the discontinuity formulation of the 3D-dual boundary element method. *Engineering Analysis with Boundary Elements*, 24:777–788, 2000.
- [46] M. Gosz and B. Moran. An interaction energy integral method for computation of mixed-mode stress intensity factors along non-planar crack fronts in three dimensions. *Engineering Fracture Mechanics*, 69:299–319, 2002.